POLITECNICO DI MILANO

Corso di Laurea Magistrale in Engineering Physics

Dipartimento di Fisica

Master of Science Thesis Work

POLITECNICO
MILANO 1863

Image charge screening effect on EuO thin films

Relatore: Prof. Giacomo Claudio Ghiringhelli

Correlatore: Prof. Dr. Liu Hao Tjeng

Candidato:

Federico Meneghin, matr. 841337

Anno Accademico 2016-2017

MAX-PLANCK-INSTITUT
FÜR CHEMISCHE PHYSIK FESTER STOFFE

The whole work presented in these pagese was carried out at the Max Planck Institute for the Chemical Physics of Solids, in Dresden, under the supervision of prof. Liu Hao Tjeng and dr. S. Altendorf.

To them goes my sincere thanks.

Siamo rimasti d'accordo [...] sul piacere di veder crescere la tua creatura, piastra su piastra, bullone su bullone, solida, necessaria, simmetrica e adatta allo scopo, e dopo finita la riguardi e pensi che forse vivrà più a lungo di te, e forse servirà a qualcuno che tu non conosci e che non ti conosce. Magari potrai tornare a guardarla da vecchio, e ti sembra bella, e non importa poi tanto se sembra bella solo a te, e puoi dire a te stesso "forse un altro non ci sarebbe riuscito".

P. Levi, *"La Chiave a Stella"*

Contents

List of Figures

Prefazione

I primi studi sul monossido di europio (EuO) risalgono a più di mezzo secolo fa, a partire dalla scoperta, da parte di Matthias et al. [1] nel 1961, della sua transizione ferromagnetica ad una temperatura di Curie di 69 K . Ciò che rendeva, e rende tuttora l'EuO così interessante, da diversi punti di vista, è il fatto che rappresenta uno dei rari casi di isolante ferromagnetico, mentre per la maggior parte degli isolanti e dei semiconduttori i meccanismi di superscambio danno origine ad un ordinamento di tipo antiferromagnetico. Dal punto di vista delle applicazioni tecnologiche, l'effetto di magnetoresistenza colossale mostrato dal monossido di europio rappresentava un'ottima motivazione per investigare un suo possibile utilizzo nella fabbricazione di memorie magneto-ottiche e modulatori magneto-ottici [2]. La scoperta, da parte di Oliver et al. [3] nel 1970, della transizione isolante-metallo ad una temperatura simile alla temperatura di Curie, rese l'EuO di estremo interesse anche dal punto di vista della ricerca fondamentale, in quanto esempio di *sistema fortemente correlato*. Tuttavia, dopo un intenso lavoro di studio e caratterizzazione dell'EuO e di tutti i materiali appartenenti alla famiglia dei calcogeni di europio (EuX), apparve chiaro che non vi è modo di innalzare la bassa temperatura di Curie fino a temperature compatibili con l'utilizzo al di fuori dell'ambiente di laboratorio. In aggiunta, la preparazione di monossido di europio puro, o dopato con altri elementi di possibile interesse tecnologico, si è rivelata un processo difficile e non adatto ad una produzione su larga scala.

Per questi motivi, divenne opinione comunemente accettata che non vi fosse la possibilità di alcuna applicazione pratica dei calcogeni di europio, e questo portò a una pausa di circa 20 anni nella ricerca su questi composti .

Negli ultimi anni si è rinnovato l'interesse verso l'EuO, principalmente a causa della crescente domanda di materiali con proprietà magnetiche uniche, in campi emergenti come l'elettronica di spin (*spintronica*) e le nanotecnologie più in generale. Il grande *exchange splitting*, circa 0.54 eV, che garantisce una *spin-filtering* di quasi il 100% [4], la struttura cristallina relativamente semplice e l'elevato valore del momento magnetico, circa 7 μ_B per ione di europio [5], sono tutte caratteristiche promettenti per una possibile applicazione dell'EuO come filtro di spin in giunzioni a effetto tunnel con materiali semiconduttori come silicio (Si) o arseniuro di gallio (GaAs), o con elettrodi metallici. Un ruolo cruciale in questo senso è giocato dalle proprietà fisiche di film sottili e superfici, un ambito in cui sono ancora molte le domande aperte; una profonda conoscenza e la comprensione dei fenomeni fisici in materiali relativamente semplici come l'EuO sono essenziali per trovare una risposta a tali domande, anche ad altre classi di materiali.

In un'ottica più ampia, la crescente domanda di miniaturizzazione e lo sviluppo di dispositivi su scala nanometrica renderà necessario comprendere, e possibilmente controllare, i differenti effetti dovuti alla forma e alla dimensione delle strutture in gioco. Le complesse eterostrutture tipiche delle future tecnologie saranno inevitabilmente influenzate da effetti di interfaccia e di superficie, e l'utilizzo materiali nuovi ed esotici sarà possibile solo con un solido background di modelli ed esempi. In questo contesto, un progetto come quello a cui questa tesi è dedicata diventa un banco di prova fondamentale, e i risultati qui esposti potranno servire per future ricerche anche su materiali o dispositivi diversi.

L'intero lavoro qui presentato è stato svolto in collaborazione con il gruppo di Fisica dei Sistemi Correlati del Max Planck Institute for Chemical Physics of Solids, a Dresda, sotto la supervisione del Prof. L. H. Tjeng e della Dott.ssa S. Altendorf. Il gruppo guidato dal Prof. Tjeng ha già condotto e pubblicato numerosi studi sulle proprietà dell'EuO. In particolare, si è ottenuta una ricetta stabile per la preparazione e la crescita epitassiale di film sottili di EuO su Yttria-stabilized zirconia (YSZ) [5]; sono state investigate le proprieta di campioni non-stechiometrici [6] e numerosi materiali dopanti come gadolino (Gd) [7], scandio (Sc) [8] e samario (Sm) [9] sono stati studiati e testati per aumentare la temperatura di Curie e modificare le proprietà di trasporto.

Lo scopo del presente lavoro di tesi è di illustrare il progetto attualmente in corso da parte del team del Prof. Tjeng , con la finalità di investigare, e possibilmente modificare, le proprietà magnetiche di un film sottile di materiale semiconduttore tramite l'interfaccia con un mezzo polarizzabile. L'EuO è stato scelto come materiale modello in quanto ampiamente studiato e caratterizzato e per la sua struttura chimica e cristallina relativamente semplice. Dal punto di vista sperimentale, il metodo per la crescita di film sottili è già disponibile e l'elevato momento magnetico può essere facilmente misurato con un dispositivo SQUID (Superconducting Quantum Interference Device).

Il primo capitolo riassume le principiali caratteristiche e proprietà fisiche dell'EuO. Vi sono descritte la struttura cristallina ed elettronica, da cui hanno origine molte delle caratteristiche che rendono l'EuO un materiale così interessante e particolare. I meccanismi fisici alla base dell'ordinamento ferromagnetico sono descritti nella seconda parte del capitolo, così come sono stati descritti da Kasuya [10]. Il capitolo 2 inizia con una panoramica sui cosiddetti *sistemi correlati*, una vasta classe di materiali a cui appartiene anche il monossido di europio. Con una breve discussione basata sul formalismo della seconda quantizzazione, viene mostrato come alcune delle principali proprietà fisiche di questi materiali dipendano da pochi caratteristici parametri. Nella seconda parte, vengono descritte l'influenza della dimensionalità sull'ordinamento magnetico, e l'effetto della carica immagine (*image charge screening*) sui parametri caratteristici dei sistemi correlati. Il capitolo 3 si concentra sulle tecniche sperimentali utilizzate per preparare i campioni, con particolare attenzione all'epitassia a fasci molecolari (MBE) e ai problemi incontrati e le soluzioni adottate nel preparare campioni di elevata qualità. Nel capitolo 4 vengono descritte le analisi e le tecniche sperimentali

utilizzate durante il progetto per monitorare, controllare ed eventualmente modificare il processo di crescita. Le tecniche reflection high-energy electron diffraction (RHEED) e X-ray photoelectron spectroscopy (XPS) sono descritte in dettaglio, a causa del loro uso intensivo durante il progetto, mentre le tecniche hard X-ray photoelectron spectroscopy (HAXPES) e X-ray reflectivity (XRR) sono solo accennate, in quanto il loro utilizzo è stato limitato a pochi particolari casi. Infine, nel capitolo 5 sono presentate le tecniche sperimentali e i resultati delle caratterizzazioni magnetiche dei campioni. Il lavoro si conclude con il capitolo 6 che contiene le considerazioni finali, una panoramica sull'intero progetto e i possibili sviluppi futuri.

Abstract

The first studies on europium monoxide (EuO) date back more than half a century, when Matthias et al. [1] discovered its ferromagnetic transition in 1961. What makes EuO so interesting from different perspectives is its belonging to the rare class of ferromagnetic insulators, while for most of semiconductors and insulators the superexchange mechanisms would lead to an antiferromagnetic configuration. From a technological perspective, the huge magneto-optical effects of EuO used to be a strong motivation to investigate this material for magneto-optical memories and magneto-optical modulators [2]. Also from the academic point of view, the interest in binary europium compounds increased after the discovery of its metal-insulator transition by Oliver et al. [3] in 1970. After massive work of study and characterization of the whole family of the europium chalchogenides (EuX), however, it turned out that the relatively low EuO Curie temperature of 69 K cannot be raised up to room temperature. Moreover, the preparation of stoichiometric or doped EuO has proven to be a challenging task and which may be not suitable for large-scale production. It was commonly accepted that there was no chance for an industrial application of this compound, and this led to a pause of about 20 years in the study and research about europium chalcogenides.
In the last years an increasing interest in EuO emerged due to the technological demand of new performing magnetic materials mainly in the field of spintronics. Its large exchange splitting, which guarantees a spin-filtering of nearly 100% [4], its relatively simple crystal structure and the large magnetic moment of about 7 μ_B per functional unit, are promising features for the application of EuO as a spin-filter tunnel barrier in direct contact with Si or GaAs and with metal electrodes. Here, the properties of thin films and surfaces play a major role, an aspect still under investigation. An understanding of physical properties in these simple binary compounds is essential for the explanation of similar phenomena in other classes of materials.
From a more general perspective, the technological demand of miniaturization and the raising of the production of nanoscale devices will make it unavoidable to deal with the interplay of different effects due to size and geometry. The complex heterostructure of future technologies will be inevitably affected by interface and surface effects, and the possibility of using new and exotic materials will be possible only with a solid background of well understood models and examples. In this context, a project like the one to which this thesis is devoted turns out to be a fundamental testing ground, and the results will enable the development of further studies also on different materials.
The whole work presented in this thesis was carried out in collaboration with the group of Physics

of Correlated Matter of the Max Planck Institute for Chemical Physics of Solids in Dresden, under the supervision of Prof. L. H. Tjeng and Dr. S. Altendorf. Many studies had already been done and many achievements were published by Dr. Tjeng and his team in the past twenty years about EuO. In particular, a reliable recipe for the growth of epitaxial and layer-by-layer EuO on Yttria-stabilized zirconia (YSZ) [5] has been developed, the physical properties of the off-stoichiometric samples have been investigated [6] and many dopants like Gd [7], Sc [8] and Sm [9] have been studied and tested to enhance the Curie temperature and to tune the transport properties. The purpose of this thesis is to present the current state of the project on EuO currently ongoing in the group lead by Prof. L. H. Tjeng. The aim is to investigate and possibly tune the properties of metal oxide thin films through the interface with metallic or non-metallic materials. EuO has been chosen as a model compound because it is well known, quite simple in its structure and components. From an experimental perspective, the know-how for film growth and sample preparation is already available and its large magnetic moment that can be easily measured using a superconducting quantum interference device (SQUID).

In this thesis, an overview on the fundamental properties of EuO is given in chapter 1. Here the crystal structure and the basic electronic structure are described, from which many of the interesting features of EuO arise. The physical mechanisms of its magnetic properties, as proposed by Kasuya [10], are described in the second part. Chapter 2 gives an overview of the so-called *correlated systems*, the large class of materials to which EuO belongs. By a basic discussion based on the second quantization formalism, it is shown how physical properties of these materials depend on a few characteristic parameters. The second part of this chapter describes how thin films are affected by these parameters, and how to handle and possibly tune them using the image charge screening effect. Chapter 3 is devoted to the experimental techniques used to prepare the samples, focusing on Molecular Beam Epitaxy as well as the main problems and solutions adopted to prepare a good quality sample. Chapter 4 is about the analysis and the experimental techniques used during the whole project to monitor, check and modify the growth process. In particular, reflection high-energy electron diffraction (RHEED) and X-ray photoelectron spectroscopy (XPS) are described in more detail, because of their massive use during the work. Hard X-ray photoelectron spectroscopy (HAXPES) and X-ray reflectivity (XRR) are simply mentioned, since their use was limited to a few particular samples. Finally, in chapter 5, the experimental technique and the results of the magnetic analysis of the samples are presented. The final considerations and an overview of the work are summarized in chapter 6.

1. Overview of EuO

1.1 Crystal structure

Europium monoxide, as the name suggests, is a compound formed by europium (Eu) and oxygen (O) atoms, arranged in a rocksalt structure. The lattice parameter is temperature-dependent with a value $a = 5.144$ Å at room temperature, which reduces to $a = 5.127$ Å below 20 K [11]. Every Eu atom is octahedrally surrounded by O atoms, and occupies the lattice sites of an FCC structure with 12 nearest (NN) and 6 next-nearest neighbours (NNN) ferromagnetically coupled.
At the surface, depending on the orientation, the Eu atom coordinations of NN and NNN are reduced to 8 and 5 for (100), 6 and 3 for (111) and to 7 and 3 for (110). This has dramatic consequences on the magnetic properties, especially for thin films as explained in chapter 2. As can be easily seen from the cell in fig. 1.1, the number of functional units (Eu atoms) per single cell is then given by F.U. $= 1 + 12 * \frac{1}{4} = 4$, and the volume of the primitive cell is simply $V_{cell} = a^3$.

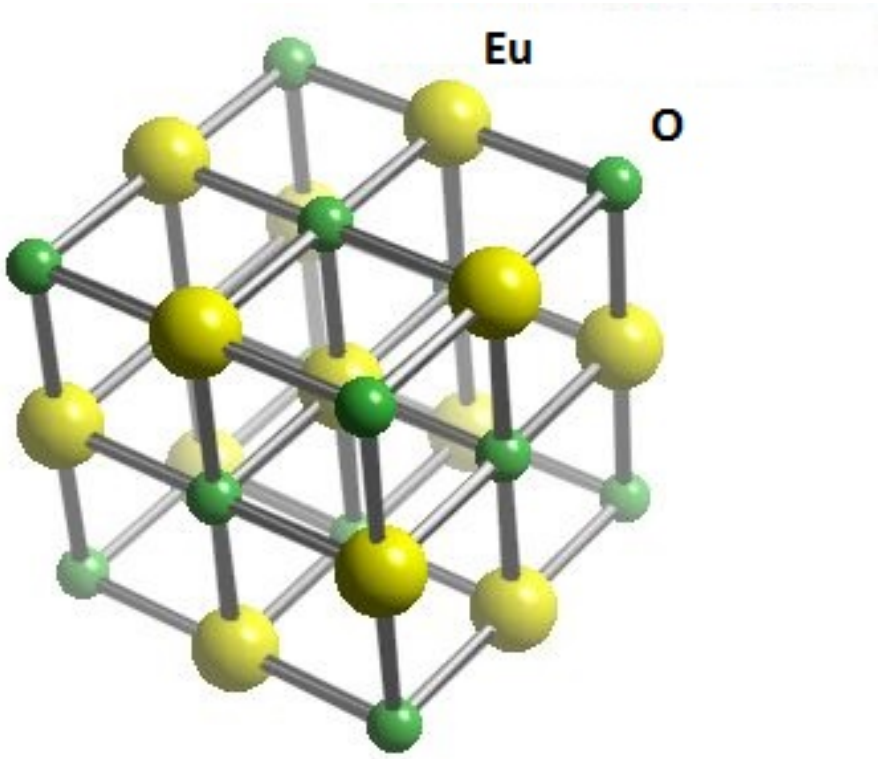

Figure 1.1: Sketch of the EuO unit cell. From [12].

1.2 Electronic structure

When forming the compound, electrons of the outer atomic shell $6s$ of Eu are transferred to the oxygen atom, that completely fills its outer $2p$ shell so that the electronic configuration is

$$\text{Eu} : [\text{Xe}]4f^7 5d^0 6s^2 \rightarrow \text{Eu}^{2+} : [\text{Xe}]4f^7 5d^0 6s^0$$
$$\text{O} : 1s^2 2s^2 2p^4 \rightarrow \text{O}^{2-} : 1s^2 2s^2 2p^6$$

This strong ionic character explains why, at room temperature, EuO is an insulator, with an optical bandgap of about 1.2 eV.

In fig. 1.2, the radial distance of the last subshells of EuO and EuS, another europium chalcogenide, is shown. The half filled $4f$ subshell is much less spatially extended compared to the filled subshells $5s$ and $5p$, therefore the main part of its charge density lies deep inside the ion. The overlap of $4f$ wavefunction between two adjacent Eu ions is almost null, and the seven $4f$ electrons can be considered as localized. Crystal field effects are negligible, and thus Hund's rules applies without quenching correction, leading to high spin configuration $S = 7/2$ and $L = 0$. Spectroscopic ground state is then ${}^8S_{7/2}$. Many calculations and different approaches have been done to recon-

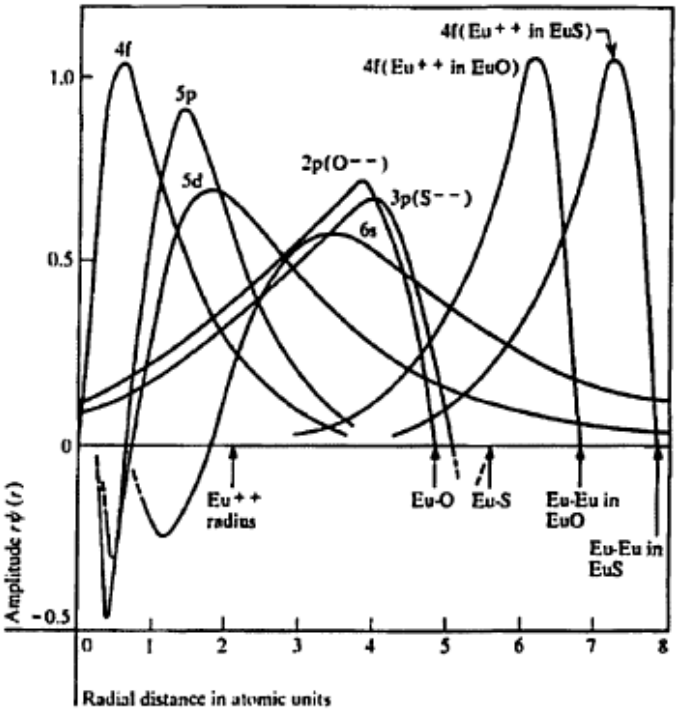

Figure 1.2: Radial extension of the outermost atomic orbitals of EuO and EuS. From [2].

struct the energy levels and electronic structure of EuO, in order to match them with experimental results. We just summarize here the results of Mauger and Godart [2], the main reference when it comes to europium calchogenides. Fig. 1.3 shows the results of the successive approximations

applied for obtaining an accurate theoretical prediction of EuO energy levels. The corresponding density of states is reported in fig. 1.3(b). The valence band is mainly formed by the $2p^6$ elec-

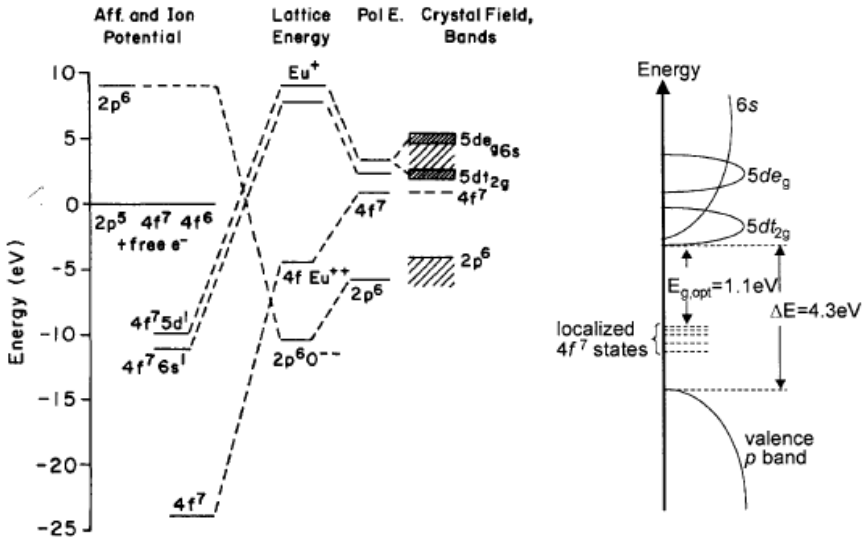

(a) (b)

Figure 1.3: a) Results of successive approximation in calculating EuO energy levels b) Schematics of the DOS of EuO. Pictures from [2].

trons of the anion, and conduction bands is formed by the $5d$ and $6p$ cation levels. The first empty level is the $5dt_{2g}$ originating from the small crystal field splitting of the $5d$ level. The $4f$ levels, as told before, are localized and are not involved in transport properties. The gap of 1.1 eV for the $4f$-$5d$ transition is then called *optical* band-gap, while the energy gap for the $2p$-$5d$ transition is of the order of 4 eV. It is worthwhile to take a closer look to the spin resolved bandstructure and energy levels of EuO, because it is one of the main reasons why EuO appears to be such a promising material for spintronics fundamental studies and research applications, if not for commercial applications. [13] Fig. 1.4(a) and fig. 1.4(b) show the band structure for spin-up and spin-down

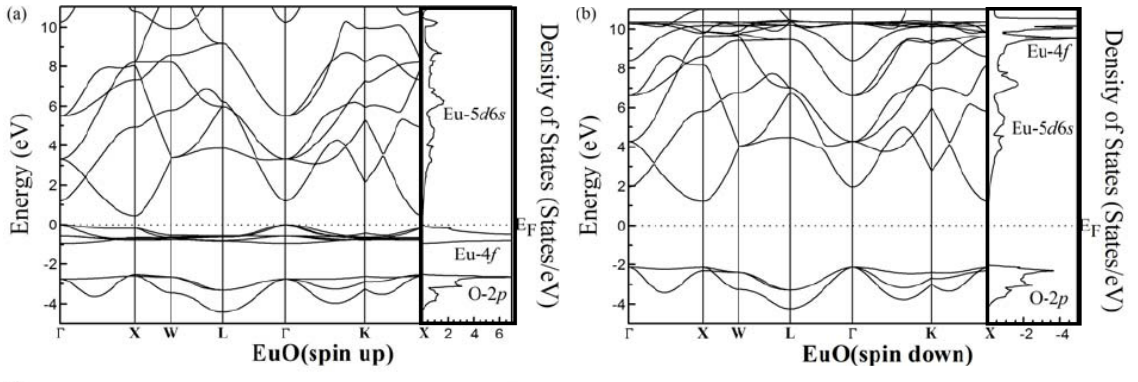

(a) Spin-up bandstructure (b) Spin-down bandstructure

Figure 1.4: spin-resolved band structure of EuO. Picture taken from [14].

electrons. In the spin-down diagram is the lack of the localized $4f$ states near the Fermi level is visible. This is obvious, since the spectroscopic ground state ${}^8S_{7/2}$ is a pure spin-up configuration. The bottom of conduction band, for spin-down electrons, is higher in energy because of the large exchange-splitting ($\Delta E_{ex} \approx 0.54$ eV) of the $5d$ levels below T_C, as shown in fig. 1.5. This $2\Delta E_{ex}$

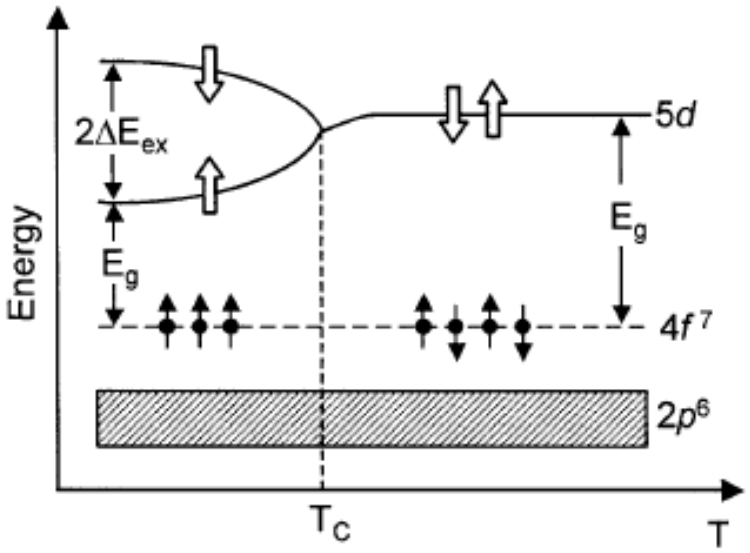

Figure 1.5: Schematic of EuO bandgap as a function of temperature. Picture from [15].

energy gap was first determined by measuring the redshift of the absorption edge in single crystals of EuO cooled below T_C [16], and it is due to the Zeeman splitting of conduction band caused by the ferromagnetic order of the $4f$ spins [17]. Because the splitting $2\Delta E_{ex}$ in bulk EuO is significant compared to E_{gap}, EuO could potentially produce a total spin polarization of $P \approx 96\%$[4], a much higher value compared to the usual ferromagnetic spin-filters [15], and could potentially be used as a spin-filter for tunnel barriers in spin-FET [18] especially when interfaced with silicon [19].

1.3 Magnetic properties

1.3.1 Heisenberg model

EuO belongs to the rare family of magnetic insulators, and this interesting property is one of the reasons of the huge amount of resarch works on this material. In stoichiometric EuO, the magnetic properties are well described by a mean field theory with an effective molecular field H_M originating from the localized $4f^7$ electrons in each Eu^{2+} ion. The highly symmetric crystal structure and its localized magnetic moments make EuO a perfect example of an Heisenberg ferromagnet,

with exchange interactions between the two localized magnetic sites i, j of the type

$$-J_{i,j}\mathbf{S}_i \cdot \mathbf{S}_j \tag{1.1}$$

where the exchange constant $J_{i,j}$ originates from the overlap of the atomic wavefunctions involved in this *direct exchange*. We can restrict our attention only to the interaction between nearest neighbour (NN), with exchange parameter J_{NN}, and next-nearest neighbours, with exchange J_{NNN}, and write an approximated Hamiltonian by splitting the two different contributions:

$$H = -\sum_{i,j} J_{i,j}\mathbf{S}_i \cdot \mathbf{S}_j \approx -\sum_{i,m} J_{NN}\mathbf{S}_i \cdot \mathbf{S}_m - \sum_{i,n} J_{NNN}\mathbf{S}_i \cdot \mathbf{S}_n \tag{1.2}$$

where the first sum extends over the (m) nearest and the second over the (n) next-nearest neighbours. The magnetization dependence on the applied magnetic field $M(H)$ shows the typical hysteresis loop of a ferromagnet (fig. 5.6), while the temperature dependence of magnetization $M(T)$ satisfies

$$M = N g_J \mu_B B_J(x) \tag{1.3}$$

where $B_J(x)$ is the Brillouin function

$$B_J(x) = \frac{2J+1}{2J}\coth\left(\frac{2J+1}{2J}x\right) - \frac{1}{2J}\coth\left(\frac{1}{2J}x\right) \tag{1.4}$$

with $x \equiv g_J \mu_B B / K_B T$, and for EuO $J = 7/2$. The ferromagnetic transition for bulk samples is at $T_{C,bulk} = 69$ K, and the saturation magnetic moment would be $M_{sat} = g_J J = 7\mu_B$. Despite the success of this approximation in explaining the macroscopic ferromagnetic properties of EuO, major problems arise when trying to theoretically derive the value of exchange parameters and to explain the physical mechanism that leads to ferromagnetic coupling. In fact, because of the highly localized character of the $4f^7$ electrons responsible for the magnetism, the direct overlap of NN wavefunctions shoud be negligible, and even more the one of NNN wavefunctions. Moreover, a pure direct exchange would lead to an *antiferromagnetic* order.

Thus, some more complex mechanisms must be considered to explain the exchange mechanism that leads to J_1 and J_2. A succesful explanation has been proposed by Kasuya [10] and is summarized here.

1.3.2 J_1 - Indirect exchange

In the indirect exchange mechanism, the anion O does not play any role, and $4f$ electrons of Eu^{2+} are coupled through their interactions with the conduction electrons. In particular, a $4f$ electron is transferred to a $5d$ state of a next neighbor cation which then polarizes the $4f$ spin through the intra-atomic exchange interaction J_{df}. The value of J_{NN} can be estimated as

$$J_1 = 2J_{df}\frac{|t_{df}|^2}{SU^2} \tag{1.5}$$

where J_{df} is intra-atomic exchange interaction constant, t_{df} is the transfer energy between d and f, and U is the energy difference between d and f, with the order of magnitude of E_{gap} [13]. The numerical value of J_1 calculated by Kasuya is of the order $J_1 \approx 3.5 \cdot 10^{-5}$ eV .

1.3.3 J_2 - Superexchange

In the superexchange interaction, the coupling is mediated by the $2p$ anion orbital. Because of the symmetry of the rocksalt crystal structure, the superexchange is of 180° type (cf. chapter 2), and originates from 3 different physical mechanisms:

- Kramers-Anderson superexchange. An f electron is transferred via oxygen p orbital to an f orbital on a neighboring atom, and becomes effectively coupled with the next-nearest neighbor f electron. This exchange is antiferromagnetic and very small, since the transfer integral t_{fp} is small and the electron-electron repulsion U_f is large ($\approx$ 11 eV). The value of this interaction is approximately $J_{K-A} \approx -0.5 \cdot 10^{-6}$ eV.

- Superexchange via the $d-f$ interaction. Oxygen electrons are transferred to the d orbitals of neighboring Eu atoms, where they affect the $4f$ spins of next-nearest neighbor via the $d-f$ exchange interaction. The 180° angle of Eu-O-Eu bond leads to an antiferromagnetic exchange and explains why the overall J_2 is negative in most of europium chalcogenides. For EuO, $J_{df} \approx -6.5 \cdot 10^{-6}$ eV.

- A mixture of both above mentioned mechanisms. Via hybridization the $5d$ and $2p$ orbitals form bonding and antibonding molecular orbitals. An oxygen electron is excited from the bonding to the antibonding $5d-2p$ molecular orbital, which interacts via the exchange coupling with both Eu spins. Its place is then taken by a Eu $4f$ electron, and the $5d$ electron fills the $4f$ hole left. This could lead to a ferromagnetic exchange, and explains why J_2 is positive in EuO. The numerical value of the constant describing this interactions is $J \approx +8.2 \cdot 10^{-6}$ eV, and such an high value is the reason why the overall $J_{superex}$ is positive for EuO.

The results for the interaction constants J_1 and J_2 are then both positive, with values

$$J_1 \approx 3.5 \cdot 10^{-5}\text{eV} \quad J_2 \approx 1.2 \cdot 10^{-6}\text{eV}$$

2. Properties of correlated systems

EuO, as well as many other rare-earth and transition metal compounds, belongs to the large class of so-called *correlated materials*, a set of physical systems for which experimental data clearly shows a breakdown of the nearly-free electron approximation and the consequent one-electron band theory. EuO, for instance, is a ferromagnetic insulator with a bandgap of about 1.2 eV [2], while the one-electron theory would predict this system to be metallic because of the partially filled f band. This, as well as many of the unexpected properties shown by correlated materials, is due to the presence of competing interactions experienced by the electrons. On the one hand, delocalization of the charge leads to a gain in kinetic energy, giving rise to the usual band structure, while on the other hand the strong Coulomb repulsion between electrons on the same site tends to avoid charge fluctuations. After having discussed the specific case of EuO in chapter 1, it is useful to introduce a general framework for these *correlated systems* and to highlight some of the basic concepts behind the experimental work carried out during the project.

2.1 A toy model

As an example of how competing interactions affect the properties of a system, an oversimplified one-dimensional model of hydrogen atoms is presented here, as it was originally proposed by Mott [20]. The starting point is an infinite chain of atoms equally spaced by a distance d, large enough to fall in the tight-binding limit [see fig. 2.1]. Each atom of this system, that we will generally call "site", can host *n* electron, and for the moment we can safely assume a single, infinitely degenerate, s-type orbital and neglect the spin degree of freedom. Let us call *N* as the total number of electrons in the system. Moving an electron from one site to another one far away would create a delocalized electron-hole pair, leaving the system in a situation like the one in fig. 2.1. If we neglect any interaction between electrons on the same site (*on-site correlation*), we are in the usual nearly-free electron approximation, where electrons move in a periodic potential determined by the positive ion cores of the lattice and the mean-field potential of all the other electrons together. Bandstructure calculations would predict this system to be a metal, with single s band and certain bandwidth *W*, dependent both on the hopping integral *t* and the lattice connectivity. But it is known from atomic physics [21] that removing an electron from one atom has an energy cost (E_I, ionization energy) that is $E_I = 13.6$ eV in case of hydrogen atom, while adding one leads to an energy gain (E_A, electron affinity), again $E_A = 0.7$ eV in case of hydrogen. Thus, moving an electron from an atom

to another one *costs* an energy $\mathrm{U} = \mathrm{E_I} - \mathrm{E_A} = 12.9$ eV, the energy of Coulomb repulsion between two electrons on the same site.

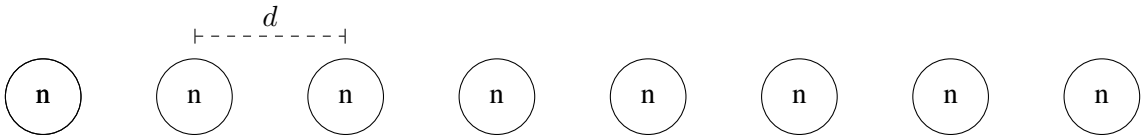

Figure 2.1: 1-D model of a Hubbard insulator.

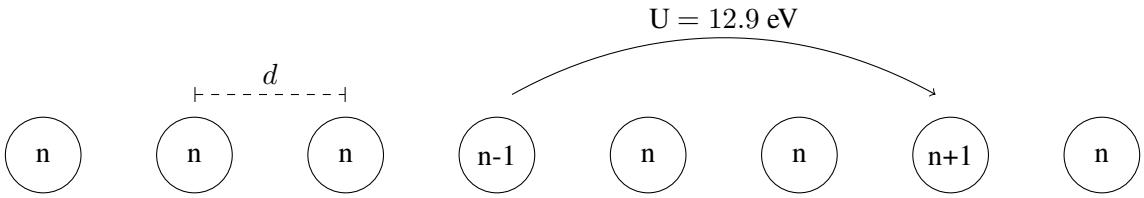

Figure 2.2: 1-D model of a Hubbard insulator. The circles are the sites that can host up to n electrons each. Moving one electron between two sites would cost an energy $U = E_I - E_A$.

2.1.1 Hubbard Hamiltonian

The easiest attempt for an analytical description of a correlated systems is to write an Hamiltonian containing this two energy terms, the potential and the kinetic one. For simplicty, we will assume that each atom involved has only one single relevant orbital. However, applying this still-idealized model to an infinite lattice requires a formalism that is independent of the number of lattice sites considered, or, in other terms, that is valid for any number of electrons. Be $|0\rangle$ the system with no electrons, we introduce the creation $c^\dagger_{i\sigma}$ and annihilation $c_{i\sigma}$ operators, that respectively puts and removes an electron with spin σ in the orbital φ_i. Thus we can write, for a single electron state

$$|\uparrow,\cdot\rangle = c^\dagger_{1\uparrow}|0\rangle \quad |\cdot,\uparrow\rangle = c^\dagger_{2\uparrow}|0\rangle$$
$$|\downarrow,\cdot\rangle = c^\dagger_{1\downarrow}|0\rangle \quad |\cdot,\downarrow\rangle = c^\dagger_{2\downarrow}|0\rangle$$

and for two-electron states

$$|\uparrow,\downarrow\rangle = c^\dagger_{2\downarrow}c^\dagger_{1\uparrow}|0\rangle \quad |\downarrow,\uparrow\rangle = c^\dagger_{2\uparrow}c^\dagger_{1\downarrow}|0\rangle$$
$$|\uparrow\downarrow,\cdot\rangle = c^\dagger_{1\downarrow}c^\dagger_{1\uparrow}|0\rangle \quad |\cdot,\uparrow\downarrow\rangle = c^\dagger_{2\downarrow}c^\dagger_{2\uparrow}|0\rangle$$

We can also introduce the *occupation number* operator $n_{i\sigma} = c^\dagger_{i\sigma}c_{i\sigma}$ whose eigenvalues describes the occupation of the i orbital electrons with spin σ. So, for example

$$n_{1\uparrow}|\uparrow,\downarrow\rangle = |\uparrow,\downarrow\rangle \quad n_{1\downarrow}|\uparrow,\downarrow\rangle = 0$$

and of course

$$n_{i\sigma}|0\rangle = 0$$

Given this set of operators, is possible to describe the competing terms in a correlated system. Indeed, the Hamiltonian describing the hopping of a spin σ electron from one orbital to another one, say from φ_1 to φ_2, is

$$H = -t(c^{\dagger}_{1\sigma}c_{2\sigma} - c^{\dagger}_{2\sigma}c_{1\sigma}) \tag{2.1}$$

where the matrix element t is the so-called *hopping parameter*, and can be intuitively interpreted as the strength of hopping from site to site. In the absence of other terms the hopping gives rise to the usual formation of bands.

The second energy scale is given by the Coulomb repulsion U between two electrons on the same atom. If this on-site Coulomb repulsion is comparable to the bandwidth, the electrons can no longer be considered independent. The double occupation of an atom is energetically very costly, and the movement of an electron will be hindered by the Coulomb repulsion. One says that the electrons move in a correlated way. The Coulomb interaction of electrons in one orbital, say φ_1, can be represented as a term

$$H = Un_{1\uparrow}n_{1\downarrow} = Uc^{\dagger}_{1\uparrow}c_{1\uparrow}c^{\dagger}_{2\downarrow}c_{2\downarrow} \tag{2.2}$$

The sum of these two terms, extended over an infinite lattice of equally spaced atoms, leads us to the famous Hubbard Hamiltonian:

$$H = -t\sum_{i,j,\sigma} c^{\dagger}_{j\sigma}c_{i\sigma} + \frac{U}{2}\sum_{i,\sigma} n_{i\sigma}n_{i\bar{\sigma}} \tag{2.3}$$

Despite being conceptually and computationally oversimplified, the Hubbard Hamiltonian cannot be solved exactly for most real 3D systems. It is still useful, however, to look at the two extreme cases, when $U >> t$ and $U \approx 0$.

For $U \approx 0$, no correlation is present, only one band is formed (we are considering the case of just 1 relevant orbital per each atom) and the system is metallic for a non complete filling of the band. In the opposite case of $U >> t$, the Coulomb interaction dominates and we recover the so called *atomic limit*, where we have a bunch of electrons distributed as uniformly as possible in the lattice, being the double occupancy of an orbital highly unfavourable. Hopping is suppressed, and the same number of electrons will give rise to an insulator. We can "recover" the band picture by saying that the Coulomb repulsion splits the half filled band into two bands, called the lower and upper Hubbard band (see in fig. 2.1.1) with a band-gap proportional to U [22]. A direct experimental evidence of such a behaviour can be obtained by performing a combination of photoemission (PES) and inverse-photoemission spectroscopy (IPES) [23], or by scanning tunnelling spectroscopy (STS) [24], or in general by any experiment sensitive to the density of states of both the valence band and the conduction band.

Moreover, in between these two extreme cases, there must be a certain critical value $U = U_c$ for which we have the transition between metallic and insulating state - the Mott transition, that is indeed observed in correlated systems like EuO [3]. Despite being idealized and not directly applicable to real situations, the Hubbard model is useful for its conceptual simplicity and gives an overview of the main phenomena to be expected in strongly correlated systems.

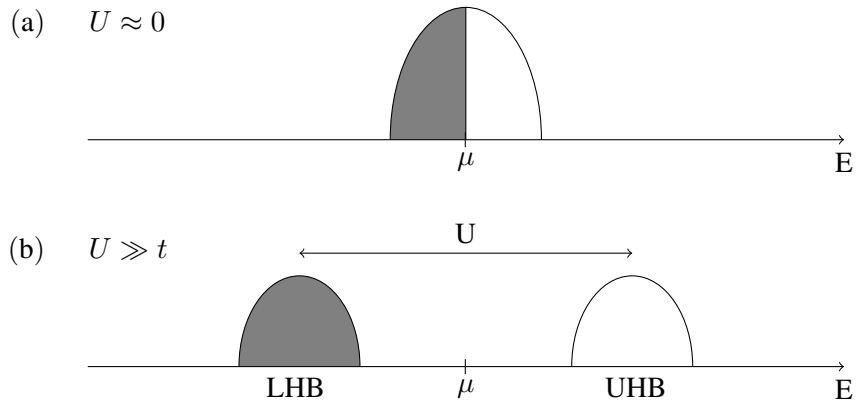

Figure 2.3: Schematic density of states expected in a combined PES/IPES experiment for a non-correlated (a) and a strongly correlated system (b).

2.2 Exchange interactions

Real situations are commonly the superposition of different effects, and a simple Hamiltonian cannot be sufficient to derive a good quantitative prediction of the main phenomena involved when describing magnetic behaviour of a material.
The complicated magnetic interactions of EuO have been described and calculated by Kasuya, a good theoretical prediction of their magnitude requires the use of the fourth-order perturbation theory. The numerical results are reported in chapter 1. The basic mechanisms leading to these results, however, can be easily sketched using the second quantization method, that also highlights their dependency on the parameters characteristics of the correlated systems. A complete discussion of this topic can be found in Koch et al. [25], and it will be summarized here.

2.2.1 Direct exchange

Direct exchange originates from the direct overlap of the wavefunctions of the orbitals involved in the magnetic interaction. For EuO, this would be the overlap between the two $4f$ orbitals of nearest neighbouring and next-nearest neighbouring Eu^{2+} ions. This is the basic mechanism considered in the the most elementary treatment of ferromagnetic coupling, despite being quite unrealistic for

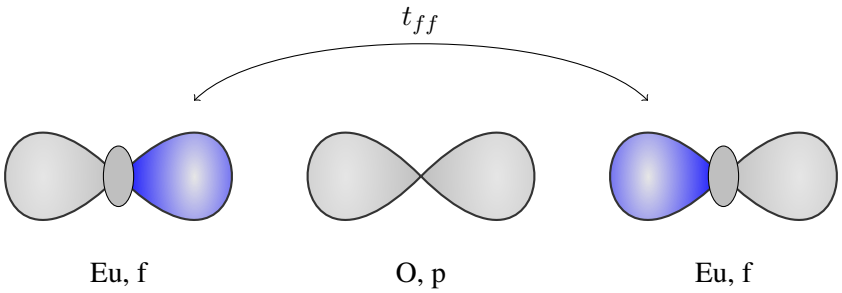

Figure 2.4: Direct exchange exchange.

most of the situations. Also for EuO, indeed, the overlap between $4f$ wavefunctions is negligible (cf. fig. 1.2), and that is the main reason why we need to discuss the physical origin of the J_1 interaction constant. Conceptually, the exchange interaction as described above is exactly the same as what we describe when speaking about the Mott toy model. Hopping between neighbouring orbitals is involved, exactly as in the Mott description, and the Hamiltonian describing *direct exchange* is the same as eq. 2.3

$$H = -t \sum_{i,j,\sigma} c^{\dagger}_{j\sigma} c_{i\sigma} + \frac{U}{2} \sum_{i,\sigma} n_{i\sigma} n_{i\bar{\sigma}} \tag{2.4}$$

In the second quantization, spin operators can be written as:

$$S^x_i = \frac{1}{2}\left(c^{\dagger}_{i\uparrow} c_{i\downarrow} + c^{\dagger}_{i\downarrow} c_{i\uparrow}\right) \quad S^y_i \quad = -\frac{i}{2}\left(c^{\dagger}_{i\uparrow} c_{i\downarrow} - c^{\dagger}_{i\downarrow} c_{i\uparrow}\right) \quad S^z_i = \frac{1}{2}\left(n_{i\uparrow} - n_{i\downarrow}\right) \tag{2.5}$$

and with this notation the effective Hamiltonian can be written in terms of the spin operators, after eq. 2.4, in the form:

$$H_{eff} = \frac{4t^2}{U}\left(\vec{S}_1 \cdot \vec{S}_2 - \frac{n_1 n_2}{4}\right) \tag{2.6}$$

the exchange intergral J_{ex} would then be:

$$J_{ex} = \frac{4t^2}{U} \tag{2.7}$$

The effective Hamiltonian is then spin-dependent, like the magnetic direct exchange. However, since the exchange constant J_{ex} is positive, the configuration with antiparallel spins have lower energy, and direct exchange, in this simple form, would lead to *antiferromagnetism*.

2.2.2 Superexchange

The *direct exchange* mechanism described above requires the overlap of the orbitals involved in the exchange. But in many ionic solids, the orbitals responsible of the magnetic moment are very localized in space, like the $3d$ orbital of many transition metal oxides and the $4f$ of EuO, so the

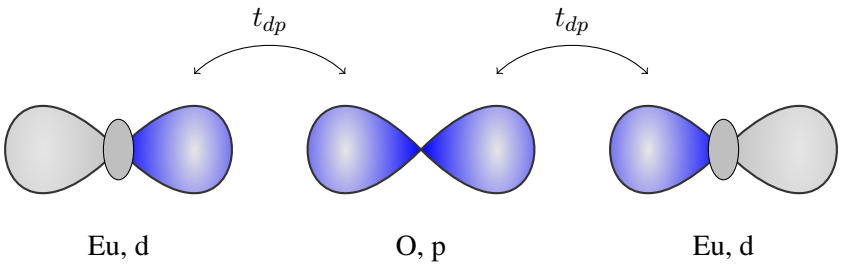

Figure 2.5: 180° superexchange between the d orbitals of the two cations, mediated by the p orbital of the oxygen ion. Hopping to the two other p obitals vanishes by symmetry.

direct overlap is negligible or completely absent. The magnetic ground states of such compounds is then a consequence of the so-called *Kramers-Anderson superexchange* (or simply *superexchange*) mechanism, an indirect and longer-range exchange in which the hopping of the electrons of the two cations happens through the p orbitals of the intermediate oxygen ion (see fig. 2.5). Usually, this interaction is favourable for an *antiferromagnetic* ground state, but certain geometries (see fig. 2.6) can actually lead to a *ferromagnetic* ground state. A set of qualitative rules for determining the sign of the superexchange mechanism have been proposed by Goodenough and Kanamori [26, 27], and situations with non-static occupation of the orbitals or with competing interactions, as in the case of EuO, leads to much more complicated situations where either ferromagnetic or antiferromagnetic ground states are possible. It is quite easy to apply the second quantization formalism to a simple model consisting of a 180° *superexchange* involving two d orbitals and one intermediate oxygen (see fig. 2.5), and from this to write an effective Hamiltonian and the consequent exchange interaction. This model was developed for transition metal oxides, where d orbitals are involved in the superexchange, but is conceptually useful also for f systems like rare-earth oxides

$$H = \sum_{\sigma} \left(\epsilon_d \sum_i n_{i\sigma} + \epsilon_p n_{p\sigma} - t_{pd} \sum_i (c^\dagger_{i\sigma} c_{p\sigma} + c^\dagger_{p\sigma} c_{i\sigma}) \right) + U_d \sum_i n_{i\uparrow} n_{i\downarrow} \tag{2.8}$$

The basic model is similar to the one described above for the *direct exchange*. Here, the operator $c^\dagger_{i,\sigma}$ creates a spin-σ electron in the d orbital at site i, where $i = 1$ stands for the d orbital on the left and $i = 2$ stands for the one on the right. Likewise, $c^\dagger_{p,\sigma}$ creates an electron in the p-orbital. ϵ_d and ϵ_p are the energy of an electron in a d or p orbital, respectively. Parameters U_d and t_{pd} are the Coulomb repulsion between two electrons in a d orbital (repulsion in the p orbital is neglected) and the hopping integral between p and d orbitals. After some calculations, it turns out that the superexchange constant for such a system can be written as

$$J_{superex} = -\frac{4t_{pd}^4}{(U_d + \Delta_{pd})^2} \frac{1}{U_d} + \frac{1}{U_d + \Delta_{pd}} \tag{2.9}$$

where the dependence on coulomb repulsion U_d and charge transfer Δ_{pd} is explicit. It is worthwhile to mention also another mechanism of superexchange, that could actually lead to a ferromagnetic

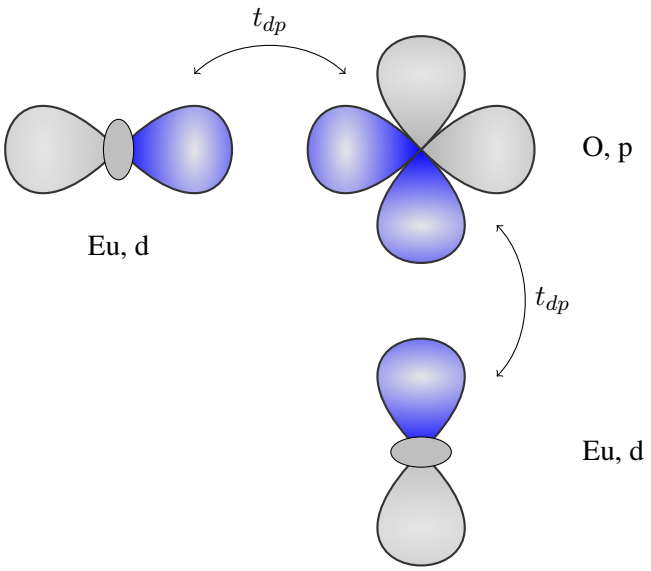

Figure 2.6: $90°$ superexchange between the d orbitals of two cations and two p orbitals of an oxygen ion. The situation is different from before, because the two p orbitals are orthogonal and there is no direct hopping of the electrons

configuration. This happens when the oxygen ion forms a 90° bridge between the d and p orbitals, as in fig. 2.6. In this case, because of the symmetry of the orbitals involved in the exchange mechanism, the effective Hamiltonian changes and the superexchange constant would be

$$J_{superex} = -\frac{4t_{pd}^4}{(U_d + \Delta_{pd})^2} \cdot \frac{2J_{xy}}{4(U_d + \Delta_{pd})^2 - J_{xy}^2} \tag{2.10}$$

slightly different with respect to eq. 2.9, but still dependent on the parameters U and Δ. In paragraph 2.4 a possible way to change parameters U and Δ is shown, and the consequences of these modifications are analyzed in chapter 5.

2.3 Effects of dimensionality on thin films

The different behaviour of materials on the nanoscale is a well known effect in many branches of physics, and especially in the world of magnetism. The atomic-scale structure of matter can usually be ignored, but when the mesoscopic dimensions of the magnetic nano-objects are comparable to some characteristic length scale, then their physical properties, and in particular the intrinsic magnetic properties such as magnetization and Curie temperature, may differ appreciably in thin films and bulk material [28]. The reduction of T_C in thin films with respect to the bulk value is a well known phenomenon, arising from either the anisotropy effect, increasing importance of spin fluctuation and lower coordination number at the surface of the material [29]. For EuO thin films, the main reason for the shift of the critical temperature T_C is the reduced coordination number of magnetic neighbours located at the EuO interfaces. The magnetic Eu^{2+} ions in the outermost layers have less magnetic neighbours than their counterparts in fcc bulk EuO, which leads to a difference between the interface and center layer magnetization.

Each Eu^{2+} ion is ferromagnetically coupled to its 12 nearest neighbours (NN) with $J_1/K_B = +0.606$ K and its 6 next-nearest neighbours with $J_2/K_B = +0.119$ K. At interfaces, in contrast, the average number of NN and NNN is reduced depending on the crystalline orientation. Eu^{2+} ions in the outermost (100) interface layer have 8 NNs and 5 NNNs, whereas in the (111) [(100)] orientation, the coordination number is reduced to (6) [(7)] NNs and (3) [(4)] NNNs.

A quantitative theory of this problem has been developed by Schiller et al. already in 1999 [30], for a $S = \frac{7}{2}$ Heisenberg ferromagnet, with an FCC crystal structure and in the form of a (100) thin film. The case fits perfectly with EuO, as is shown in chapter 1, and the same authors indeed applied their theoretical model to EuO thin films [31] showing the predicted behaviour of T_C as a function of the number of monolayers n. Their results are graphically shown in fig. 2.7.

Experimental observations, however, show a noticeable deviation with respect to this theoretical predictions [18]. In particular, the Curie temperatures of the experimental data are shifted to lower values, especially for EuO layers thinner than $t \approx 2$ nm. This finding suggests that the short-range ferromagnetic NN and NNN coupling at interfaces of real substances is lowered compared to ideal systems. The authors suggested that in the case of realistic EuO thin films imperfect interfaces can reduce the average number of magnetic neighbours even further.

From the structural point ov view, the presence of a finite interface roughness can lead to structural disorder, as the Eu^{2+} ions may be randomly distributed over the lattice sites of the cation sublattice. Moreover, oxidations of part of EuO films can also enhance the difference between the ideal and the real case, as Eu^{2+} ions can readily oxidize to non-magnetic Eu^{3+}. It has been shown in [32] that the stable non-magnetic compound Eu_2O_3 is mainly localized at the interfaces, and thus it

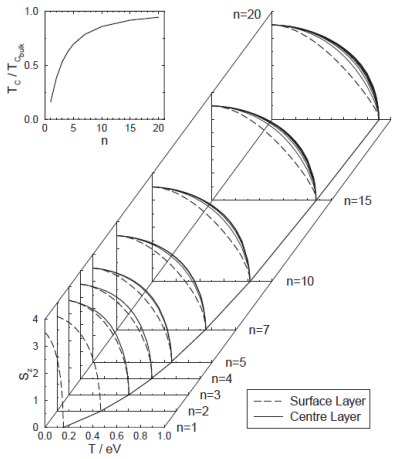

Figure 2.7: Results of the calculations carried out in [31], where is shown the dependency of T/eV on the number of monolayer. The inset shows the behaviour of T/T_C.

might account for the lowering of average short-range magnetic order. In chapter 4, however, it is explicitly shown that there is no formation of Eu_2O_3 at the interface between the layer of EuO and Mg/MgO, but the edges of the EuO which are not covered with Cr or Mg/MgO might oxidize when exposed to air for the *ex-situ* measurements.

All these effect cannot be disregarded in real systems, and they very likely account for the lower Curie temperature compared to theoretical predictions. Fig. 2.8 shows the results in literature for the Curie temperature of EuO thin films of decreasing thicknesses. As a definition of Curie temperature, the inflection point of the $M(T)$ curve has been chosen, and the same we did for our project (cf. chapter 5)

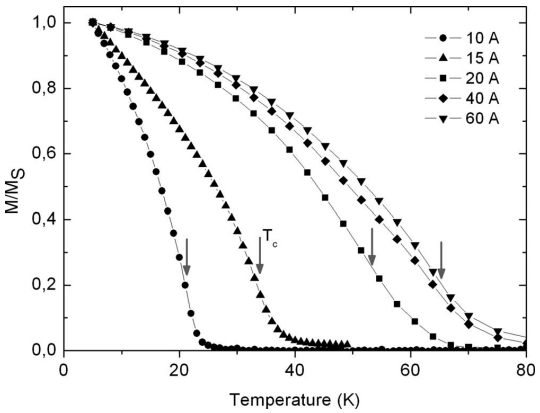

Figure 2.8: Experimental data from [18] of $M(T)$ for samples of various thickness.

The problem of the thickness dependence of T_C can be discussed in a simple way on the basis of the mean-field theory, with $K_B T_C$ being proportional to the ferromagnetic ground state energy: $K_B T_C \approx \sum_i z_i J_i S^2$.

The transition temperature $T_C^{surf}(n)$ for n EuO monolayers scales with the average number of

magnetic neighbours z_i according to:

$$T_C^{surf}(n) = T_C^{bulk} \frac{z_{NN} J_1 + z_{NNN} J_2}{12 J_1 + 6 J_2}. \tag{2.11}$$

Here, z_{NN} and z_{NNN} are the average numbers of nearest neighbors, coupled by J_1, and NNNs, coupled by J_2, which depend on the total number of EuO monolayers n. The differences between the surface and center layer coordination lead to the final expression for the layer-dependent magnetization:

$$T_C^{surf}(n) = T_C^{bulk}(1 - \frac{c}{n}) \tag{2.12}$$

where c is a numerical parameter.

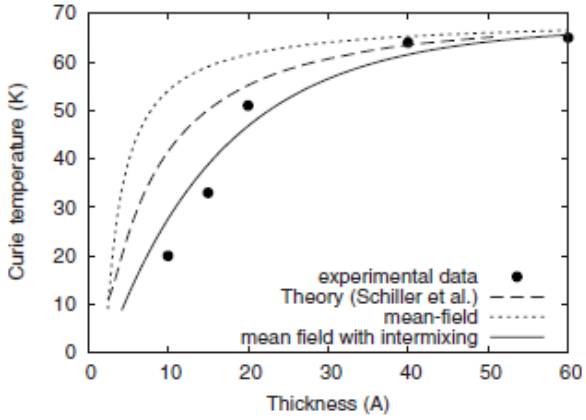

Figure 2.9: Different fittings of experimental data for the temperature dependence of T_C. Data from [18].

2.4 Thin films and image charge screening

The core of this project is based on the observations contained in a series of papers by S. Altieri and L. H. Tjeng [33][34] [35], where they propose and experimentally observe that ultrathin oxide films may have modified chemical-physical properties when interfaced with metal substrates, or metallic layers, because of image potential screening due to charge fluctuations.

As described in the previous chapter, in strongly correlated systems the basic electronic structure, band gaps and exchange interactions are mostly determined by a few fundamental quantities. Among these, the on-site Coulomb interactions U in the open cation shell, the charge transfer energy Δ, meaning the energy cost to transfer one electron from the O $2p$ to the cation shell, and the one electron band widths. When U and Δ are larger than the band width, the oxide will be a magnetic insulator, for which the nature and the magnitude of the conductivity gap are determined by the relative importance of U and Δ.

Because of the inverse proportionality to U and Δ of the strength of exchange interactions (eq. 2.7, 2.9, 2.10), these will be considerably enhanced if ways could be found to strongly reduce U and Δ. This can be used, and verified, by the observation of a different Curie temperature in ultrathin oxide films interfaced with metals, such as EuO interfaced with Mg. When the one electron band widths are larger than U and Δ, then the effects of electron correlation become negligible and the material properties are mostly determined by electron delocalization and hybridization effects, and usual band theory applies. Duffy and Stoneham predicted that in such a case the image potential will enter the energetics of the system and reduce U considerably [36]. This is illustrated in fig. 2.10 showing an ionic lattice for which the open-shell cation site is defined as the energy required for the charge excitation $2(n) \rightarrow (n+1) + (n-1)$, where (n) is the valence of the cation in the ground state.

U, for a lattice of isolated ions, is given by:

$$U = E_I^{cat} - E_A^{cat} \tag{2.13}$$

where E_I^{cat} is the ionization potential and E_A^{cat} the electron affinity of the cation. Close to the metal

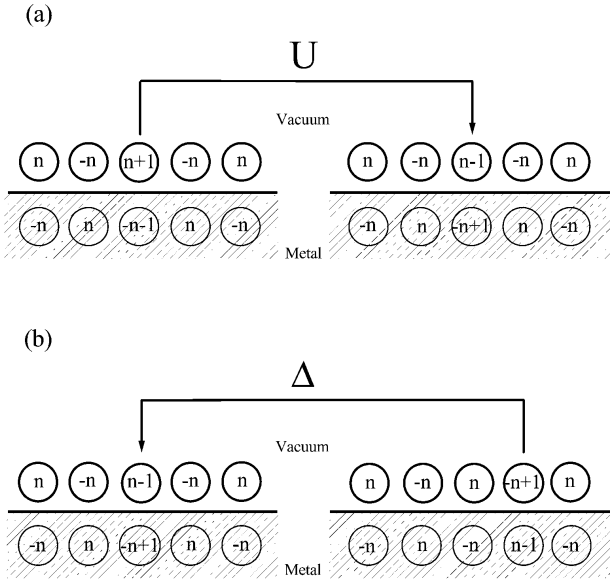

Figure 2.10: Graphical representation of the effect of image charge screening on U and Δ, from [37].

surface, all the ionic charges are subject to the interaction with the metal that can be described as an effective interaction with image charges appearing below the metal surface.

The creation of the additional positive (negative) charge on the cation is then accompanied effectively by the simultaneous creation of an additional negative (positive) image charge in the metal. The energy of the charge excitation that defines U is given by the total energy of two cations with charges $n+1$ and $n-1$, minus the total energy of the cations in the ground state with both charges

(n), and in the presence of image charges it is altered into:

$$U = E_I^{cat} - E_A^{cat} - (n+1)^2 E_{image} - (n-1)^2 E_{image} + 2n^2 E_{image} \tag{2.14}$$

where the third and fourth terms describe the total image charge stabilization energy of the two cations in the excited state, and the fifth term that of the two cations in the ground state. Here E_{image} is defined as the binding energy of a unit charge with its induced image charge, and is a positive quantity. The result is now that U is reduced by two times the unit image charge energy:

$$U = E_I^{cat} - E_A^{cat} - 2E_{image} \tag{2.15}$$

They argue that D will also be similarly reduced and could be smaller than in the bulk depending on the change in the Madelung potential.This is illustrated in fig. 2.10, showing the charge excitation that defines Δ, namely $(n) + (-n) \rightarrow (n-1) + (-n+1)$ where (n) is the valence of the cation and $(-n)$ of the anion in the ground state.The energy cost is given by:

$$\Delta = -E_A^{cat} + E_I^{an} - e\sum_{i\neq 0} V_i - e\sum_{i'\neq 0} V_{i'} + e\sum_{j\neq 0} V_j + e\sum_{j'\neq 0} V_{j'} - 2(n-1)^2 E_{image} + 2n^2 E_{image}. \tag{2.16}$$

Here the third and fourth terms describe the cost in energy when an electron (charge -e) is added at the cation site $(i = 0)$ due to the Madelung potential set up by all other ions $(i \neq 0)$ and their images $(i' \neq 0)$, i.e. all the image charges except the one of cation. Similarly, the fifth and sixth terms are the cost in energy when an electron is removed from the anion site $(j = 0)$ due to the Madelung potential set up by all other ions $(j \neq 0)$ and their images $(j' \neq 0)$.

The last two terms represent the change in the stabilization energy in the final and the ground states due to the image charges of the cation and anion involved in the charge excitation process considered.

The image charges of all the other ions are static with respect to the excitation, and therefore their energy contributions can be described as originating from a Madelung like potential. For the cation $-eV_{i'=0} = 2nE_{image}$, and for the anion $-eV_{j'=0} = 2nE_{image}$, where the factor of two accounts for the fact that the energy associated with an induced charge is half of that for a static charge. The expression for Δ can be rewritten as:

$$\Delta = -E_A^{cat} + E_I^{an} - e\sum_{i\neq 0} V_i - e\sum_{i} V_{i'} + e\sum_{j\neq 0} V_j + e\sum_{j'} V_{j'} - 2E_{image}. \tag{2.17}$$

In other words, the Madelung potentials that contribute to Δ for a thin ionic film on a metal are now equal to those for a double film consisting of the ionic film plus its static image film. Thus, if the Madelung potentials of such a film are not too different from those in the bulk materials, the Δ of a thin film on a metal will be smaller by $2E_{image}$ as compared to that of the bulk.

3. Film Growth

3.1 Molecular Beam Epitaxy - MBE

Every study about thin films, surfaces, interfaces and many other related fields have the unavoidable need of good quality and parameter-tunable samples, for which the comparison between theoretical predictions and experimental results would be meaningful and useful for a correct understanding of the physical properties of the system. Among the various techniques for materials deposition and film growth, Molecular Beam Epitaxy (MBE) has proven to be the most reliable and versatile one, and stands now as the state-of-art tool for fundamental research and applications in many areas of nanoscience [38].

In MBE, the growth of the film is achieved under Ultra-High Vacuum (UHV) conditions by evaporation and condensation of selected materials on an ordered substrate surface with a controlled temperature. The materials to be grown are physically transported from the source to the substrate in the form of a thermal-energy beam of atoms or molecules, and depending on the process they can remain unchanged or undergo chemical reactions. Several elements can be evaporated simultaneously from different crucibles, and the composition of the growing layer depends on the relative arrival rate of the constituent elements; mechanical shutters can abruptly interrupt each beam, so that the process can be controlled on the atomic scale. A quartz crystal monitor is usually inserted in the chamber to monitor in real-time the arrival rate of the evaporated materials. A schematic setup of an MBE chamber is depicted in fig. 3.1. The MBE chamber we used for the deposition of oxide ultrathin film is shown in fig 3.2. It is equipped with two oxygen valves that enable the growth of materials in an oxygen environment. In this way, also oxide materials such as EuO and MgO can be grown. Obviously, since chemical reactions are expected during the growth, the recipe for the growth of each material must be carefully determined and optimized. The detailed conditions for achieving stoichiometric EuO and MgO are discussed in the next paragraph. The characteristic signature of MBE with respect to other deposition techniques, such as Vapor phase or Liquid phase epitaxy, is the highly precise control of the growth process. Both stoichiometry and morphology can then be monitored and tailored according to the needs.

UHV conditions are a demanding feature for every MBE system, but enable the growth to be carried out far from thermodinamic equilibrium and to be mainly determined by the kinetics of the surface processes, instead of being governed by diffusion processes occurring in the crystallyzing material near the substrate. Moreover, UHV is also the perfect environment for most electron-related

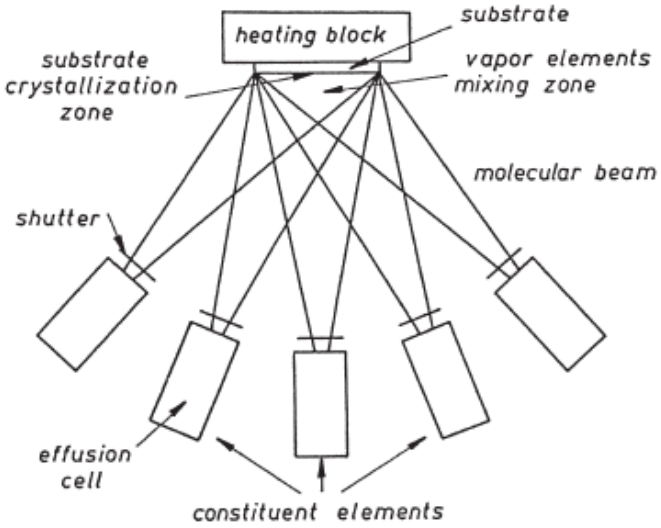

Figure 3.1: setup of a basic MBE chamber. Picture from [39]

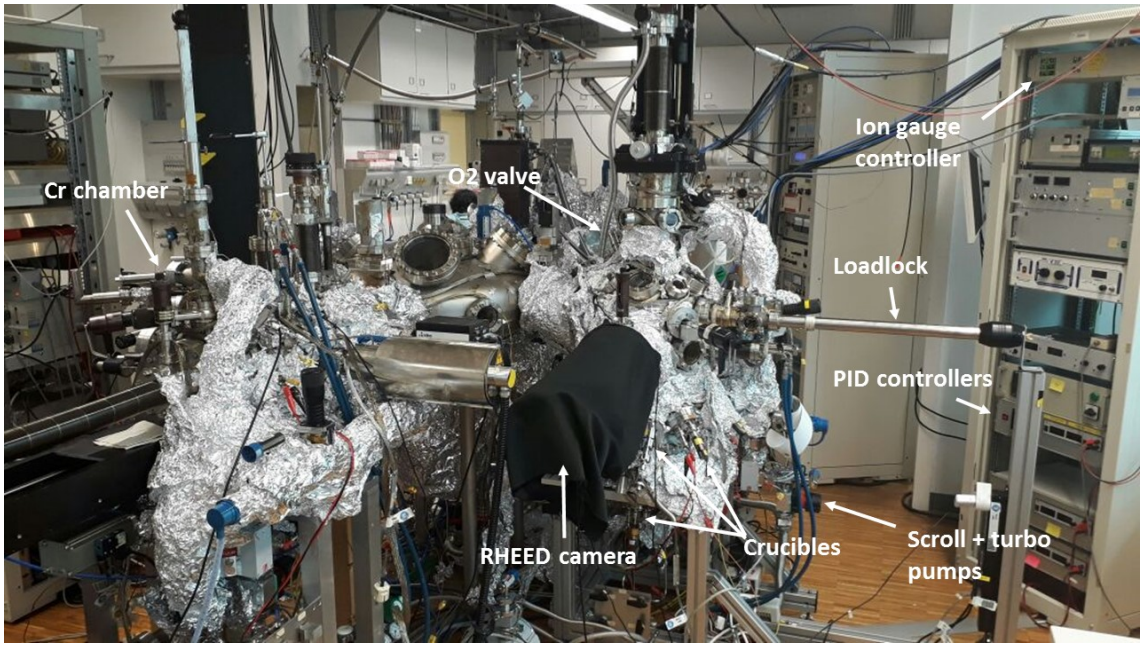

Figure 3.2: MBE chamber at the MPI for Chemical Physics of Solids, in Dresden, where the samples were grown.

analysis such as surface scattering and many types of electron spectroscopies like XPS, Auger and ARPES, that can be indeed performed *in situ* after custom modification of the basic UHV apparatus. It is not by chance that the development and the spread of MBE as a standard technique has followed the improvement of the UHV technologies over the last 40 years. [38]

3.1.1 Basic processes and growth modes

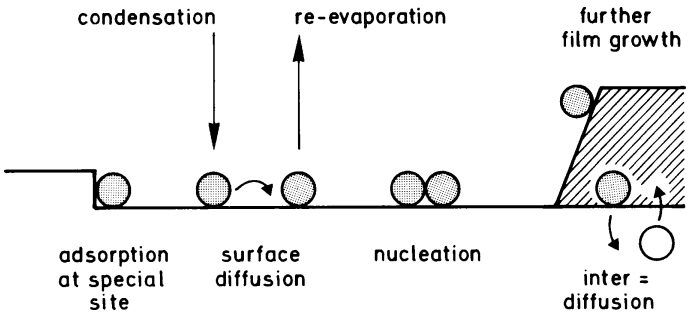

Figure 3.3: schematics of the different processes involved in the film growth on the substrate. Picture from [40].

As stated in the previous section, in MBE the cystal growth is determined by the kinetics of the various processes happening when the impinging atoms of the evaporated material interacts with the substrate surface. Among these processes, the most relevant are the ones depicted in fig 3.3:

i) adsorption of atoms or molecules impinging on the substrate

ii) surface migration and/or dissociation of the adsorbed molecules

iii) incorporation of the adsorbed molecules into the lattice substrate

iv) thermal desorption of atoms or molecules not incorporated into the crystal lattice

The kinetic of these processes is heavily dependent on the atomic species involved, the temperature of the surface, the pressure in the chamber, the impinging rate and the temperature of the evaporated material. This allows a large control of the growth, but also makes it almost impossible to achieve a fully comprehensive and reliable quantitative analysis. It is more useful, instead, to give a qualitative description of the different types of growth modes, and try to understand under which condition each mode can be obtained. Experimentally, the three main growth modes that are reported in fig. 3.4 have been observed. The first one, reported as **(a)** in the figure, is the so-called **Vollmer - Weber**, or island growth. If the mutual interactions between the deposited atoms are stronger than interactions between these and substrate, then small clusters are formed directly on the surface and the growth proceeds with conglomerations of atoms into islands of the condensed phase. On the opposite side stands the **Franck - van der Merve**, or layer-by-layer growth, indicated

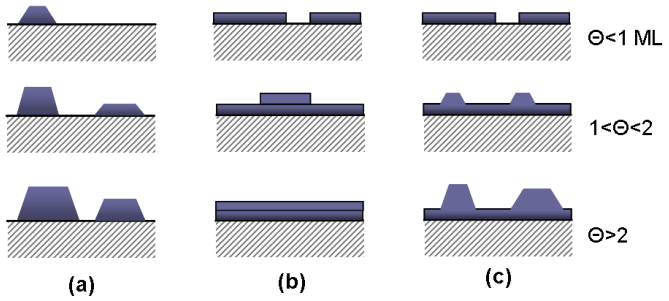

Figure 3.4: Vollmer - Weber (a), Franck - van der Merve (b) and Stranski-Krastanov (c) growth modes. The parameter Θ represents the coverage of the substrate, in units of MonoLayers (ML). Picture from [41].

as **(b)**. Interactions between adsorbate and substrate are much stronger compared to the previous case, so that the impinging beam condenses in form of a flat layer, and the subsequent new layer starts to grow only when the previous one has been completed. In between these two extremes, the so-called **Stranski-Krastanov**, or layer-plus-island, growth mode is often observed **(c)**. After one, or even several monolayers have been formed, the interaction between adsorbate atoms and the substrate gradually loose importance and what dominates the process are the mutual interactions between the atoms of grown material. This can lead to a change in the growth mode, going from the layer-by-layer to the island mode.

3.1.2 Surface tension and leading parameters

In addition to qualitative observations, it is useful to define a few quantitative parameters, in order to better understand the growth process and how it is affected by external (and controllable) variables. First of all, we have to define a surface as the interface between a solid phase and a vapor one, both homogeneous and in thermodynamic equilibrium with each other, as in fig 3.5. The intermediate

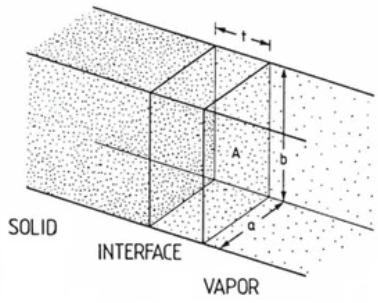

Figure 3.5: representation of a surface as intermediate layer between a solid and a vapor homogeneous phases. From [40].

layer, that we have called surface (or interface), is then a strongly inhomogeneous system with still a well defined volume and number of particles, so that all the thermodynamic properties (temperature, free energy, chemical potential per particle, etc.) have their usual meaning. The pressure *p* is the only quantity whose definition requires particular care, being the surface an inhomogeneous phase. If we consider indeed the force per unit area (i.e. the pressure) across a plane parallel to A, than the value is constant for any possible plane and well defined by the relation $F_{\parallel} = pab$. If we now consider the force across a plane *perpendicular* to A, like the plane defined by *b* and *t*, then it is no more true that $F_{\perp} = pbt$, but the real value is different from the ideal one by a certain amount. Generally speaking, it is possible to account for this difference by introducing a new parameter γ, the so-called **surface tension**, for which the relation is modified as $F_{\perp} = pbt - \gamma b$. Thermodynamic relations show that this ad-hoc parameter γ is nothing else than an excess free energy per unit area, which takes into account the reversible work needed for the formation of a new unit-area surface at a constant system volume, temperature and chemical potential.

The physical origin of an energy cost per unit surface comes mainly from the cost of breaking bonds between neighbouring atoms, in order to expose them to vacuum. This means that even for defect-free and purely crystalline materials, the parameter γ strongly depends on the orientation of the surface with respect to the bulk, because this implies a different number of bonds to be broken, different charge compensation of the new surface (that can be either polar or non-polar) and eventually surface reconstructions.

The theoretical requirement of minimizing the surface energy for an area A:

$$\int_A \gamma(\mathbf{n}) dA = minimum \tag{3.1}$$

can be graphically addressed by using the so-called Wulff plot, as the one in fig. 3.6. In this representation, the curve $\gamma(\mathbf{n}) = \gamma(hkl)$ is plotted in polar coordinates in the form of $\gamma(\theta)$, where θ is angle describing the orientation between a fixed direction and the normal to the (hkl) plane. The length $|\gamma(\theta)|$ for a given value θ is then magnitude of the surface tension in that particular direction. A set of planes, the so-called **Wulff planes**, can be constructed as the planes perpendicular to each radius vector at its intersection with the $\gamma(\theta)$ curve. By connecting the lattice planes at the minimum surface tension, it is possibile to graphically fulfill the condition (3.1) and to obtain the equilibrium shape of the crystal. If the material is liquid or amorphous, then the surface tension $\gamma(\mathbf{n})$ is isotropic and both the Wulff plot and the equilibrium shape are spherical. Once defined the quantity γ, we can carry out a simple formal distinction between the various growth modes previously described in terms of this parameter. Since γ can actually be regarded as a force per unitary length of a particular interface, the equilibrium (see fig. 3.7) is described by the so-called **Young equation**:

$$\gamma_S - \gamma_{S/F} - \gamma_F \cos\phi = 0 \tag{3.2}$$

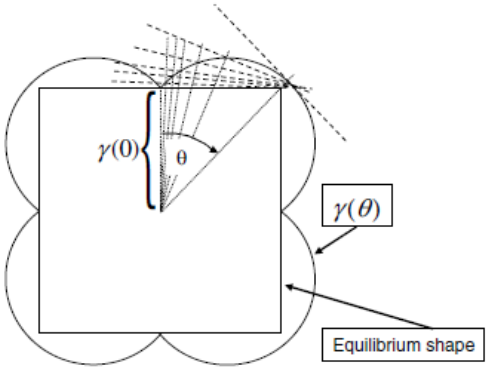

Figure 3.6: Wulff plot. From [39].

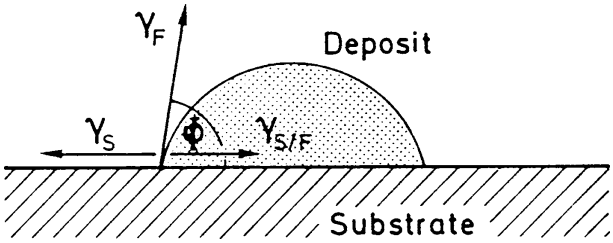

Figure 3.7: Droplet of deposited material on a surface, with the different γ parameters. From [40].

where γ_S, $\gamma_{S/F}$ and γ_F are the surface tension values for the interfaces between substrate/vacuum, substrate/film and film/vacuum respectively. The angle Φ here represents the contact angle, and is a measure of the wettability of a surface. The distinction between the three growth modes described before is clear now. For layer-by layer growth (FM), the contact angle is $\Phi = 0$, while for island growth (VW) $\Phi > 0$. These relations are the same used for describing the wetting of a liquid on a solid substrate, but for MBE process the situation is slightly different. For correct equilibrium conditions, indeed, one must also consider the gas phase surrounding the deposited material. If the gas particles overcome a vapor-solid phase transition at a pressure p, then the variation of free energy can be written as:

$$\Delta G = n\Delta\mu = nkT\ln(p/p_0) \tag{3.3}$$

where μ is the chemical potential per unit particle and p_0 is the equilibrium vapor pressure for which $\mu_{solid}(p_0, T) = \mu_{vapor}(p_0, T)$

The conditions for FM or VW growth can then be properly rewritten as:

$$\gamma_S \geq \gamma_{S/F} + \gamma_F + CkT\ln(p/p_0) \qquad \text{layer-by-layer} \tag{3.4a}$$

$$\gamma_S < \gamma_{S/F} + \gamma_F + CkT\ln(p/p_0) \qquad \text{island mode} \tag{3.4b}$$

According to this simple model, then, the growth mode is not only dependent on the substrate/material coupling, but is also on the ratio $\xi = p/p_0$, called degree of **supersaturation**. With the increasing

of supersaturation ξ, layer-by-layer growth is favored. For vacuum deposition, the actual vapor pressure p is determined by the arrival rate of impinging particles, and supersaturation ξ can reach values up to 10^{20}. In case the substrate is kept at high temperature, as in the case of EuO distillation, much lower values are achieved. The maximum value of supersaturation can also be limited by the need of a controlled stoichiometry of the grown material, a problem that cannot be considered in this simple picture but that plays a fundamental role especially for the growth of oxide materials. The easiest and most effective way to check what kind of growth mode is ongoing during an MBE experiment is the use of *in-situ* electron diffraction techniques, which will be described in detail in chapter 4.

3.2 Sample preparation

To explore the effect of the screening, a special sample layout has been designed. It is crucial, indeed, that any difference between EuO interfaced with metal or EuO interfaced with non metal is observed **in the same sample**. As described before, MBE offers many degrees of freedom that can be tuned to achieve the desired result, but the drawback is that every sample is the result of a unique combination of these variables. Any comparison between different interfaced material is meaningful only if all the other variables are strictly the same, a condition that can be achieved best on the same EuO film. The standard layout of the samples to be analyzed is reported in fig. 3.8. As a substrate, we chose to use Yttrium-Stabilized Zirconia (YSZ), that has a lattice constant

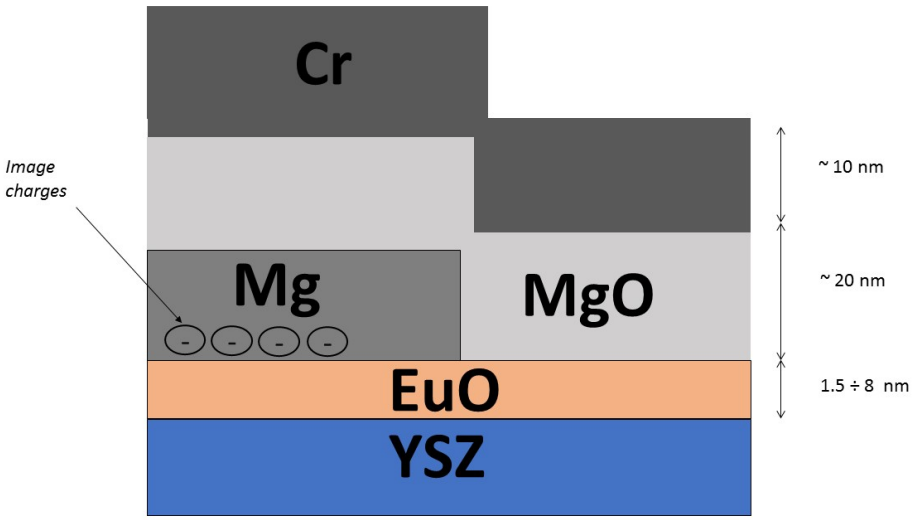

Figure 3.8: design of the standard sample grown in the MBE chamber.

of 5.142 Å , nearly identical to the 5.144 Å value of EuO at room temperature. We can define a

lattice mismatch as [42]:

$$f = \frac{a_{sub} - a_{Eu}}{a_{sub}} \tag{3.5}$$

according to which value the growing layer would be subject to compressive ($f < 0$) or tensile ($f > 0$) strain. For EuO on YSZ, lattice mismatch is tiny ($f = 0.3\%$), and epitaxy has been already reported in previous studies [43][5]. The preparation of a sample can be divided in 5 main steps, a preliminary one and one for each of the materials to be grown.

3.2.1 Substrate and plate preparation

YSZ substrates are supplied by SurfaceNet GMBH in the form of $10\times10\times0.5$ mm^3, epi-polished along the (100) plane. They are cleaned in an ultrasonic bath with acetone and isopropanol. Two parallel chromium stripes are deposited in an auxiliary MBE chamber, in order to avoid charging effects during XPS analysis. They are then mounted on a tantalum, or stainless steel plate, where a mask of the same material was previously welded. Substrates are then inserted in the main vacuum chamber, with a base pressure $P \approx 2 \cdot 10^{-10}$ mbar. Such a low base pressure is achieved using a cryopump, and is measured by an ion gauge. Once in the chamber, the substrate is annealed for ca. 180 minutes in an oxygen atmosphere, with $P \approx 5 \cdot 10^{-7}$ mbar, at a temperature $T_{annealing} = 600\ ^\circ C$, in order to get rid of all the possible impurities and surface contaminations. After the annealing, the substrate is ready for the EuO deposition.

3.2.2 EuO deposition

The recipe for obtaining stoichiometric EuO using MBE, the so-called *Eu distillation method*, is well known [5] and is described in detail in P. Steeneken PhD dissertation [43]. Since we used a different MBE setup, the growth parameters have to be tuned to meet the Eu distillation conditions. Before mounting the annealed substrate on the manipulator, the europium metal flux rate was checked and kept at a constant value of about $8-8.5$ Å/min. Since the flux rate of the beam is exponentially proportional to the crucible temperature, this was kept under control by a PID controller at a value $T_{Eu} = 559-565$ °C. The key point of the distillation method is the re-evaporation of excess europium metal. Without this condition, off-stoichiometric Eu-rich samples can be prepared, with different physical properties [43]. The substrate was initially kept at a constant temperature $T_S = 400$ °C, that is enough for the re-evaporation of excess Eu. After some trials, however, we observed that $T_S = 420$ °C allowed a better surface mobility and a better crystal growth (cf. fig. 4.5 with 4.6). All the last samples have been prepared at $T_S = 420$ °C.

The molecular oxygen needed to the formation of EuO was supplied through a leak valve on top of the chamber, and its pressure and composition were monitored using both an ion gauge and a

commercial Quadrupole mass spectrometer by Pfeiffer Vacuum. For the distillation method, we experimentally determined an oxygen pressure of about $P_{O_2} = 3.5 \cdot 10^{-8}$ mbar.
Once the europium flux rate, substrate temperature and oxygen pressure are all stabilized to their reference value and the substrate is in the correct orientation for the RHEED analysis, the europium shutter is opened, and the growth starts. Growth is monitored in real-time with RHEED, and a video of the diffraction pattern on the phosphorous screen is recorded for the RHEED oscillations analysis (fig. 4.8).
By calculating the period of the RHEED oscillations, it is possibile to determine the growth rate of the layer (see chapter 4) using the equation:

$$\text{thickness} = \frac{a_{Eu}}{2 * T_{osc}} * \text{time} \tag{3.6}$$

Once the correct thickness is reached, growth is terminated by closing abruptly the oxygen leak valve. After 15-20 seconds, the europium shutter is closed too, and the substrate is cooled down to room temperature.

3.2.3 Magnesium, magnesium oxide and chromium deposition

The tantalum or stainless steel mask is then applied to the sample in order to grow a thicker layer (ca. 20 nm) of magnesium metal on about half of the area. The effect of image charge screening, if present, would be visible in this half of the sample, because here the conduction electrons of the magnesium metal are almost free to rearrange at the interface to form the image charge. During magnesium and magnesium oxide growth, the sample has to be aligned with the crucible in such a way that the mask is effective, to achieve the geometry in fig. 3.9. This means that the sample cannot be aligned with the RHEED electron gun, and real-time monitoring of the growth is impossibile. The conditions for the growth of magnesium and magnesium oxide has been tested in previous samples, and ad-hoc XPS analysis shows no degradation of the underlying EuO layer (cf. fig. 4.17). Mg metal is grown with the substrate kept at room temperature, with the crucible at $T_{Mg} = 258 - 264$ °C for a growth rate of about 4-5 Å/min. As for Eu, the temperature was adjusted for each sample to reach a similar and stable value for the growth rate. After around 20 minutes of pure Mg deposition, the mask is removed and another film of about 20 nm of MgO is grown on top of the sample. The substrate is still kept at room temperature, and Mg temperaure is the same as for Mg metal deposition. The oxygen valve is opened after ca. 15 seconds, and the growth is carried out with an oxygen pressure $P_{O_2} = 7.8 - 8 \cdot 10^{-8}$ mbar. MgO growth was terminated after around 35 minutes by closing at the same time the oxygen valve and the magnesium shutter. Figure 3.9 shows a top-view of a sample after this third step of the process. The whole sample is then moved to another smaller vacuum chamber, where is capped with a layer of 10 nm of chromium to avoid

contamination and overoxidation of the underlying materials during *ex-situ* analysis. Chromium is evaporated at $T_{Cr} = 1120$ °C for around 20 minutes. Table 3.1 reports an overview of the most significant samples grown, their growth conditions and the analysis done on each of these.

sample	EuO		Mg/MgO		analysis	thickness	remarks
	T(°C)	P_{O_2}(mbar)	T(°C)	P_{O_2}(mbar)			
TRY04	562	$3.5 \cdot 10^{-8}$			XPS, XRR	46nm	EuO+Cr
S802	564	$3.5 \cdot 10^{-8}$			XPS, HAXPES	55nm	EuO
S803	561	$5 \cdot 10^{-8}$			XPS, HAXPES	55nm	Eu_2O_3
FM02	567	$5 \cdot 10^{-8}$			XPS	15nm	Eu_2O_3 reference
FM03	560	$3.5 \cdot 10^{-8}$			XPS	15nm	EuO reference
FM18	555.5	$3.8 \cdot 10^{-8}$			XPS, RHEED	15nm	EuO
SA006	563	$3.5 \cdot 10^{-8}$			XPS, SQUID	5nm	EuO+Cr
SA008			262	$7.5 \cdot 10^{-8}$	XPS, SQUID		Mg+MgO+Cr
SA009					XPS, SQUID		Cr
FMA08	560.5	$3.5 \cdot 10^{-8}$	261.5	$7.5 \cdot 10^{-8}$	XPS, SQUID	6nm	
FMA14	563	$3.5 \cdot 10^{-8}$	261.5	$7.5 \cdot 10^{-8}$	XPS, SQUID	2.5nm	
FMA15	562	$3.5 \cdot 10^{-8}$	262.5	$7.5 \cdot 10^{-8}$	XPS, SQUID	3nm	
FMA17	562	$3.5 \cdot 10^{-8}$	264.5	$7.5 \cdot 10^{-8}$	XPS, SQUID	1.5nm	

Table 3.1: Overview of the growth conditions for the most significant samples

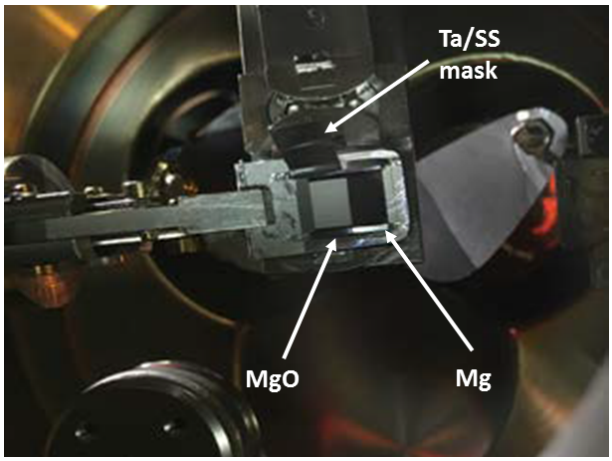

Figure 3.9: Top view of a standard sample after the third step of the process

4. Sample Analysis

4.1 Surface scattering - RHEED

As stated in chapter 3, the easiest and most effective way to monitor the crystalline growth of a layer during an MBE process is to use electron diffraction techniques. Reflection high-energy electron diffraction (RHEED) is one of the most powerful and less invasive techniques, and is now a routinely used tool in surface physics experiment. The experimental setup for RHEED characterization is commonly already integrated in MBE systems. The basic setup of a RHEED experiment, depicted in fig. 4.1, involves an electron gun, a series of tunable electronic optics and a fluorescent screen.

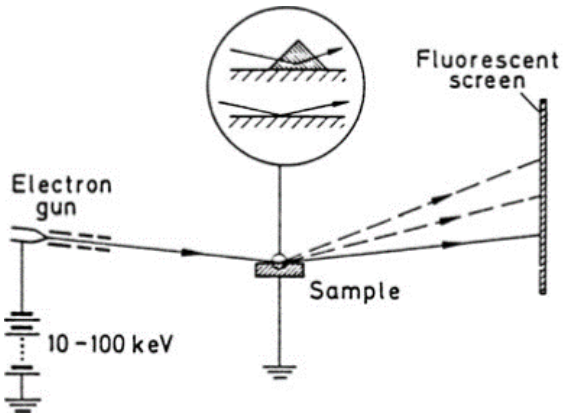

Figure 4.1: Standard experimental configuration for RHEED. Picture taken from [40].

The electron beam is accelerated and focused by the optics on the sample surface at a very grazing angle. In our case, we used an incident beam with energy $E_{e^-} = 15\ kV$ and an angle $\theta \approx 3°$. Our MBE facility was supplied with the EK-35-R RHEED system from STAIB Instruments (see fig. 3.2). The fluorescent screen was recorded by a CCD camera, and a commercial EE2000 software was used to acquire and analyze the images.

Incident electrons diffract from atoms at the surface of the sample, and a small fraction of them interfere constructively at specific angles forming regular patterns on the detector. The interference pattern depends mainly on the position and the arrangement of atoms on the sample surface, since the grazing angle enables the penetration of only few atomic layers. From the investigation of the features and the intensity recorded by the detector, a RHEED experiment can provide both

qualitative and quantitative informations. Getting quantitative informations from RHEED patterns requires the formalism of the *dynamic theory of scattering*, that describes the multiple scattering of the incident electrons before escaping the sample and being detected on the screen. For the qualitative analysis needed in everyday laboratory experiments, it is sufficient to consider only the so-called *kinematic theory*, that will be briefly described in the next paragraph.

4.1.1 RHEED kinematic theory

A geometrical interpretation of the diffraction pattern can be obtained with a discussion based on the single-scattering approximation of the incident electrons, including both elastic and inelastic scattering events. The interaction of particles with the solid can be described [40], in general, by a time-dependent potential

$$V(\mathbf{r}, t) = \sum_n v(\mathbf{r} - \mathbf{R_n}(t)) \tag{4.1}$$

where $\mathbf{R_n}(t)$ is the time-dependent displacement of the single atom on the surface (or immediately below the surface), at the primitive lattice point defined by the vector $\mathbf{n} = (m, n, p)$. In a non-relativistic approximation, a monochromatic beam of incident particles (electrons, for RHEED) with energy E_0 is associated with a wavevector $\mathbf{k}_0$ through the relation $E = \frac{\hbar^2 k_0^2}{2m_e}$, and after the scattering events the electrons are diffracted into a state with energy E' and wavevector **k'**.
Time-dependent perturbation theory enables to calculate the scattering probability, per unit time, from $\mathbf{k}_0$ into **k'**, that is composed of an elastic (no energy loss) and inelastic term (energy loss due to a single scattering event). From the elastic term it is possible to derive the condition that relates the incident and diffracted wavevectors $\mathbf{k}_0$ and **k'** with an arbitrary reciprocal lattice vector of the solid **g**:

$$\mathbf{k'} - \mathbf{k}_0 = \mathbf{g}. \tag{4.2}$$

This condition is equivalent to the Laue condition obtained when considering the X-ray diffraction from a bulky crystal structure, and it allows the construction of the usual Ewald sphere [44]. However, because of the grazing angle used in a RHEED experiment, the perpendicular component $\mathbf{k}_{0,\perp}$ of the incident wavevector $\mathbf{k}_0$ corresponds to energies well below 1000 eV, meaning that the penetration depth of incident electrons in the perpendicular direction can be less than 10 Å.
This is the reason for the high surface sensitivity of RHEED, and enables us to approximate the sampled volume with a two-dimensional layer. The reciprocal lattice then can be represented in the Ewald construction as a set of one-dimensional rods along the z-direction (see fig. 4.2). The Laue condition perpendicular to the surface is relaxed, and eq. 4.2 reduces to:

$$\mathbf{k'}_{\parallel} - \mathbf{k}_{0,\parallel} = \mathbf{g}_{\parallel} \tag{4.3}$$

According to eq. 4.3, then, sharp peaks will appear at the intersections between the Ewald sphere and the reciprocal lattice rods. When the 2D approximation is not valid anymore, the bulk condition is recovered, and the rods are slowly transformed in the usual points of the Ewald construction, as in fig. 4.2. Inelastic scattering condition can be derived in the same way, and the result is simply:

$$\mathbf{k'}_{\parallel} - \mathbf{k}_{0,\parallel} = \mathbf{g}_{\parallel} + \mathbf{q}_{\parallel} \tag{4.4}$$

where $\mathbf{q}_{\parallel}$ is the wavevector of the characteristic excitation of energy $\hbar\omega(\mathbf{q}_{\parallel})$.

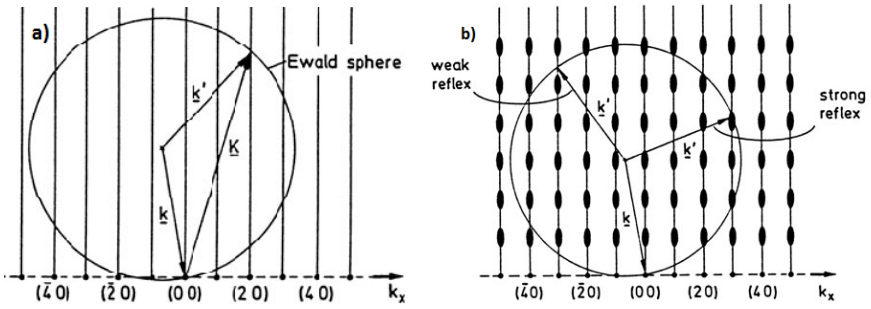

Figure 4.2: Ewald construction for in the 2D layer approximation. The constructive interference happens for the intersections between the Ewald sphere and the reciprocal lattice rods. If the 2D approximation is relaxed, the Ewald construction transforms as in fig. (**b**), until the bulk situation is completely recovered. Images from [40].

The Ewald construction for elastic scattering in RHEED requires a particular care. Because of the high energies involves in RHEED, indeed, the radius of the Ewald sphere is of the order of tens of Å^{-1}, much bigger than the rods separation. In fact, for an incident energy of 15 kV:

$$\lambda \approx \frac{12.3}{\sqrt{15000}} = 0.1 \text{ Å} \quad k_0 = \frac{2\pi}{\lambda} = 63 \text{ Å}^{-1}$$

whereas the spacing of the rods in the Ewald construction is $g = \frac{2\pi}{2.572} \approx 2.44 \text{ Å}^{-1}$, if we assume a (100) surface of EuO with a surface mesh of about 2.572 Å. These estimations show that the intersection of the large Ewald sphere with the low-spaced rods is not sharply defined, as in fig 4.2, but rather broad, as in fig. 4.3, resulting in a diffraction pattern of equally spaced streaks elongated along the normal to the shadow edge, and lying on the Laue circles [37].

4.1.2 RHEED analysis

RHEED patterns were recorded with a CCD camera and monitored via a PC using a commercial EE2000 software. The usual procedure started with an acquisition of the RHEED pattern of the substrate only, already heated to 400 °C (420 °C, after the recipe modification) and in the oxygen environment. This acquisition is needed to check the quality of the substrate before the growth,

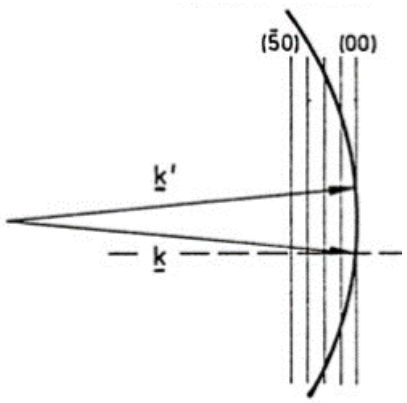

Figure 4.3: Ewald construction for a RHEED experiment. The Ewald sphere intersect lattice rods in a broader region with respect to fig. 4.2. Image from [40].

and to compare the spacing of the diffraction streaks of the substrate with the one of EuO layer that is going to be grown. However, being YSZ a large-gap insulator, the electron beam was subject to a strong charging effect, giving a blinking image on the phosphorous screen which made the RHEED pattern difficult to be recorded. The electron beam was then kept at a constant angle, and the intensity of the specularly reflected beam was recorded. In the meanwhile, RHEED images were saved at regular intervals of time; fig. 4.4 shows three RHEED patterns corresponding to three different stages of the growth of the sample FM18. The first image on the left shows the annealed YSZ substrate, where the spacing between the streaks is due to the crystal structure of the substrate. After 12 minutes of deposition, another image was acquired. Now the pattern on the phosphorous screen in only due to the growing EuO layer; the spacing between the streaks is equal to the one in the image of the substrate, and this is the indication of a good epitaxial growth due to the almost null lattice mismatch. Another image was recorded shortly before the end of the growth, after 25 minutes of deposition; the pattern is almost unchanged, meaning the process is continuing without a change in the growth mode.

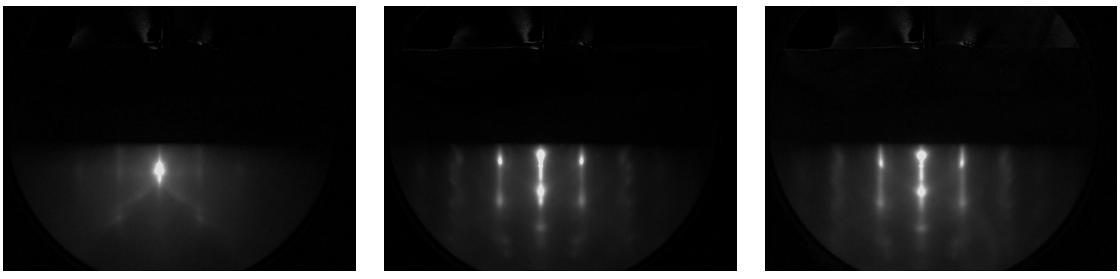

Figure 4.4: RHEED images of EuO on YSZ (001) (FM18) sample before growth, after 12 minutes deposition and after 25 minutes deposition

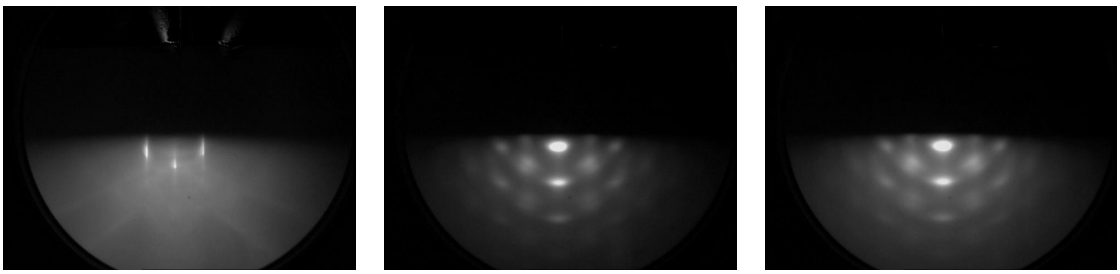

Figure 4.5: RHEED images of EuO on YSZ (001) (FMA02) sample before growth, after 25 minutes deposition and after 40 minutes deposition

The RHEED patterns of other samples grown with the same conditions of $P_{O_2} = 3.8 \cdot 10^{-8}$ and $T_S = 400°$, however, show a much lower crystal quality and a worse epitaxial growth. In fig. 4.5, for instance, three acquisitions on the sample FMA02 are shown. The YSZ substrate before the growth still shows good diffraction streaks, with the correct spacing, but the two patterns of EuO after 25 minutes and after 40 minutes of deposition show a worse growth, with the spots typical of islands formation and the complete absence of streaks. As described in the chapter 3, the following samples were prepared with a higher substrate temperature and a lower oxygen pressure. This modification stabilized the stoichiometry and improved the growth quality by allowing a better surface mobility, as shown by the patterns of the samples FMA08 and FMA11 both grown with $T_S = 420°$ C and $P_{O_2} = 3.5 \cdot 10^{-8}$ mbar.

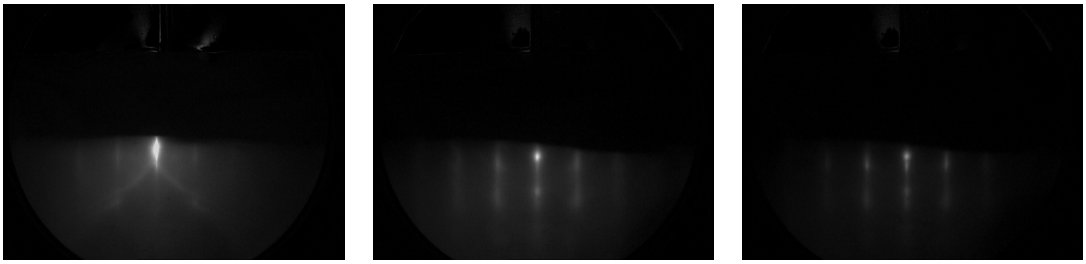

Figure 4.6: RHEED images of FMA08 sample before growth, after 6 minutes deposition and after 10 minutes deposition

4.1.3 RHEED oscillations

Another useful way to use the RHEED for obtaining information about the crystal growth during an MBE experiment is to monitor the intensity on the screen of the specularly reflected beam. During the growth process, indeed, it is possible to observe intensity oscillations with a regular period, the (**RHEED oscillations** (cf. fig. 4.8). The value of this period can be measured, and gives useful

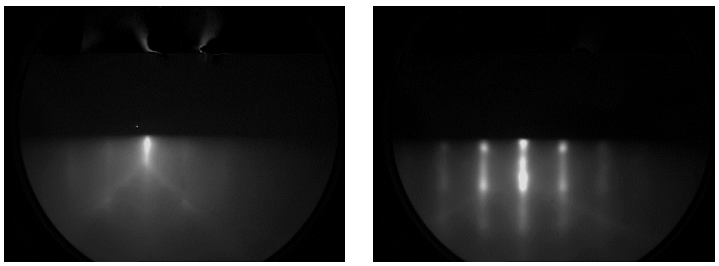

Figure 4.7: RHEED images of FMA11 sample before growth and after 6 minutes deposition. The growth time was only 7 minutes and 30 seconds, so there was no need nor time to acquire another image

informations about the growth rate and the thickness of the film.

To understand the physical origin of these oscillations, it is enough to consider the growth process: In an ideal Franck - van der Merve (FM) growth (cf. fig. 3.4), when a full atomic layer is completed, the surface is nearly flat, and the reflection from this perfect 2D layer leads to an intensity maximum of the specularly reflected RHEED beam. Further deposition of material on the surface leads to irregularly distributed aggregates of atoms (called *islands*), before the new atomic layer is completed. In between two complete layers, then, a certain disorder is present on the surface, giving a decrease in the intensity of the specularly reflected RHEED beam. By counting the number of maxima in the intensity vs. time curve of a particular Bragg spot, it is possible to monitor the number of deposited layers. The period of the oscillations, together with the knowledge of the crystal structure, enables to calculate the growth rate, and the presence itself of RHEED oscillations is a clear sign of a good layer-by-layer growth. For EuO, if we consider a growth along the (100) direction, we can clearly distinguish 3 atomic layers within a single unit cell (cf. fig. 1.1); the bottom one, the middle one and the top one, that will be the bottom one of the next layer. All these layers are formed by 4 europium atoms and 4 oxygen atoms. Maxima in RHEED oscillations will happen when each one of these layer is completed, so we will have 2 intensity maxima per unit cell. Therefore, to calculate the thickness of the growing layer, or the time needed for growing a film of a given thickness, we can use the equivalence:

$$\text{thickness (Å)} = \frac{a(\text{Å})}{2 * T_{osc}} * \text{time(s)} \tag{4.5}$$

In order to set-up the process and optimize the recipe for the growth, we did some trials of long-time deposition of EuO on YSZ. Fig 4.8 shows the intensity oscillations for two trial samples, whose recipe is reported in tab. 4.1.

Oscillations are visible for the whole time of the growth, and their period is constant and around 30 seconds. However, as it is shown in Sutarto et al. [5], the initial stages of the growth of EuO on YSZ are driven by the release of oxygen by the substrate, and only after this initial stage the growth

is actually driven by the supplied oxygen.

For the very thin films grown during the project, RHEED oscillations were more difficult to record, and growth time was often so short that there was no clear distinction between initial stage and sustained growth. Moreover, the little modifications in the growth recipe reported in par. 3 slightly affected the oscillations period, from around 30 seconds to 28 seconds. Successive XRR analysis confirmed this value (see paragraph 4.4).

sample	EuO		time
	T(°C)	P_{O_2}(mbar)	
FM12	554	$3.8 \cdot 10^{-8}$	30 min
FM18	555.5	$3.8 \cdot 10^{-8}$	30 min

Table 4.1: recipe for the growth of the samples FM12 and FM18. Successive samples, grown with a slightly lower P_{O_2} and a higher T_S, showed a small decrease of the oscillations period from 30 to 28 seconds

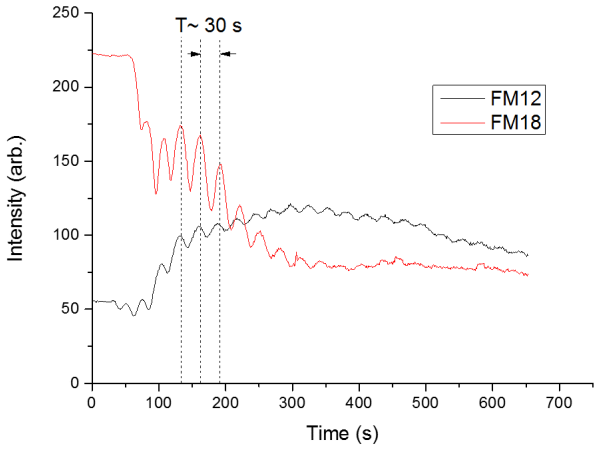

Figure 4.8: Intensity vs. time plot of the recorded oscillations for test samples FM12 and FM18

4.2 X-Ray Photoelectron Spectroscopy - XPS

4.2.1 Principles and experimental setup

The main source of information about the chemical composition and the stoichiometry of the samples was the XPS device, that allowed *in-situ* analysis of every sample immediately after the growth and without the risk of contaminations and surface degradation. The basic setup and the working principle of a photoemission experiment are shown in fig. 4.9. For XPS, the X-ray source is usu-

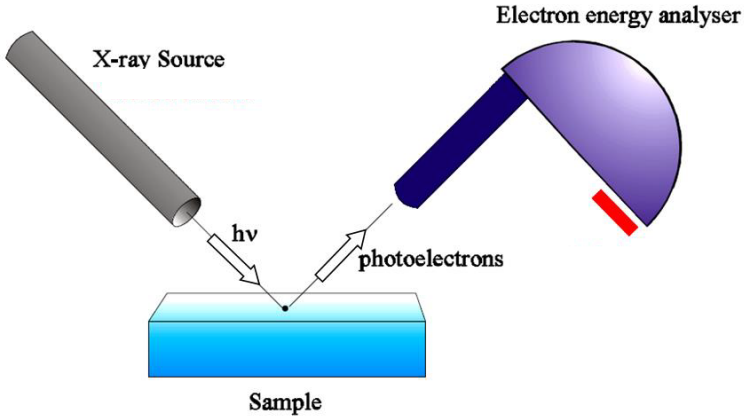

Figure 4.9: basic setup of a photoemission experiment, from [45]. For XPS, the source was an anode plate with a photon energy $h\nu = 1486.7$ eV. For HAXPES, the source was a synchrotron radiation with energy $h\nu = 6.5$ keV.

ally an anode plate, that provides, together with some dedicated optics and monochromators, an almost monochromatic X-ray beam focused on the sample. In our case we used a standard Al K_α radiation ($h\nu = 1486.7$ eV). When a photon within this energy interacts with a material, the most probable physical process to happen is photoemission; light-generated electrons (photoelectrons) are emitted from the sample, whose kinetic energies are described by the famous Einstein relation:

$$h\nu = |E_B| + \phi + E_{kin} \tag{4.6}$$

An hemispherical energy analyzer normal to the sample surface collects the photoemitted electrons, and by measuring their kinetic energies and knowing the experimental conditions (the work function ϕ) it is possible to reconstruct the orginal energy levels $|E_B|$ of the electrons in the solid, as shown in fig. 4.10; here, $|E_B|$ is defined as the distance (in energy) from the core level to the Fermi energy. The energy distribution of electrons is a unique feature of each material, so a detailed spectrum enables to determine the elements present in the sample and to univocally determine its chemical composition. It is crucial that the whole experiment is carried out in vacuum ($P_{max} \approx 10^{-10}$ mbar), so that the photoemitted electrons retain their kinetic energy can be cor-

rectly analyzed and that the sample surface is clean because of the very small probing depth. An intermediate chamber connects the MBE chamber with the XPS one, so the whole sample preparation and chemical analysis was done *in-situ* under UHV conditions. Special care must be taken when considering equation 4.6; by this description, and by fig. 4.10, it seems that the result of a photoemission experiment is dependent on the material workfunction ϕ_{sample}. When an electron is photoemitted from the sample, its kinetic energy is referred to the vacuum level of the sample itself, and the description is correct. But as soon as the photoelectron is collected by the analyzer, the contact potential (generated by the electric field due to $\Delta\phi = \phi_{sample} - \phi_{spec}$) modifies his kinetic energy, that from this moment on is referred to the vacuum level of the spectrometer. For the analysis of the kinetic energies, then, the workfunction to be considered in eq. 4.6 is ϕ_{spec}.

The calibration of ϕ_{spec} was done by measuring the Fermi edge of a reference silver sample, and

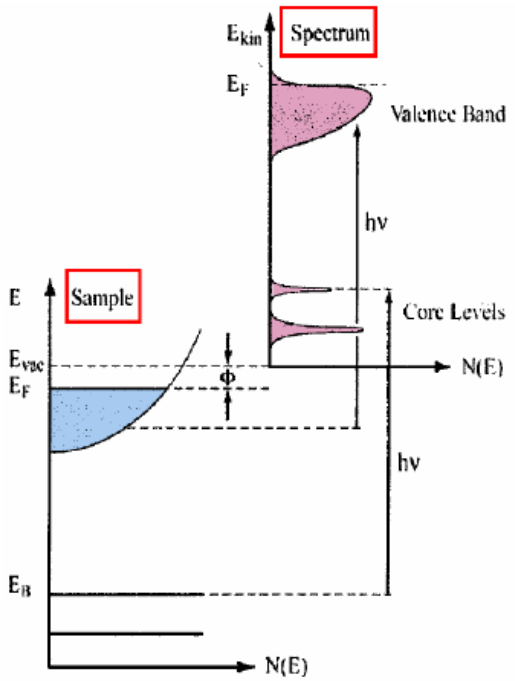

Figure 4.10: One electron picture of a PES experiment. On top there is spectrum obtained as a function of the kinetic energy of the photoelectrons, while the bottom one represents the situation in the sample, with the core (atomic) levels approximated as Dirac deltas and the valence band with the usual parabolic approximation. The ϕ in this picture ϕ_{sample}. Picture taken from [45].

by determining the Fermi energy fitting the experimental data with a Fermi function (fig. 4.11). For an electron at the Fermi edge, $|E_B| = 0$, so $\phi_{spec} = h\nu - E_{kin}$; in our case, $\phi_{spec} \approx 4.4$ eV, and this is the value that we used for the whole successive analysis. The other important aspect to highlight of XPS is its sensitivity: X-rays, even at this range of energies, penetrates quite deeply in the material, so they are able to excite electrons in the bulk of the sample. However, the electron mean free path inside a material is dependent on the energy and follows a quasi-universal curve

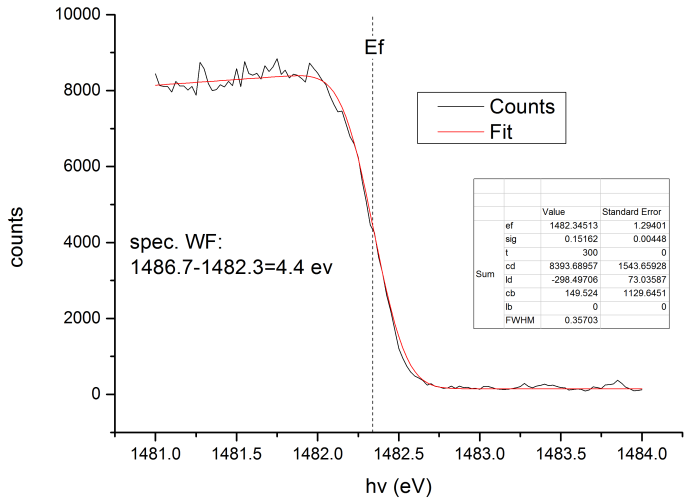

Figure 4.11: XPS of the Fermi energy region of the reference silver sample.The experimental curve is shown in black, and the red curve is the fitting with a Fermi function used to get the Fermi energy $E_F = 1482.3$ eV.

(fig. 4.12), and for the energy range of the *in-situ* XPS facility it is about $\lambda_{MFP} = 15 - 20$ Å. This means that electrons photogenerated inside the sample at a distance from the surface deeper than 15-20 Å are not able to escape from the sample, and therefore are not collected by the analyzer. Only the electron generated in the surface of the sample are detected, and every information about chemical composition in an XPS experiment is only related to surface composition. Fig. 4.13 shows the in-house XPS facility with the hemispherical Scienta SES-100 analyzer used for the project.

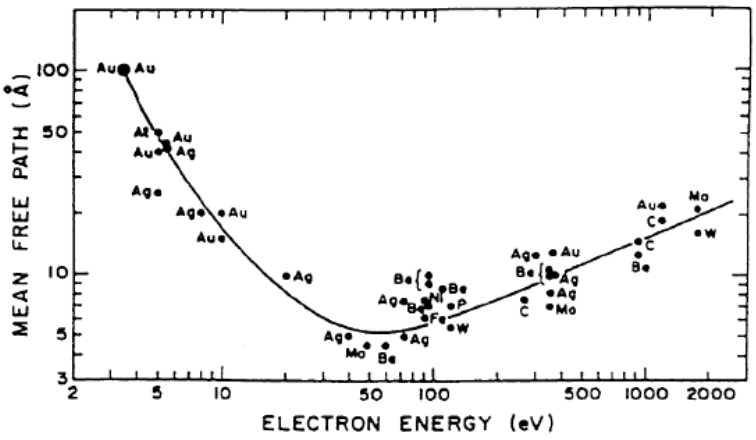

Figure 4.12: Universal curve of electrons escape depth as a function of energy. Picture taken from [46].

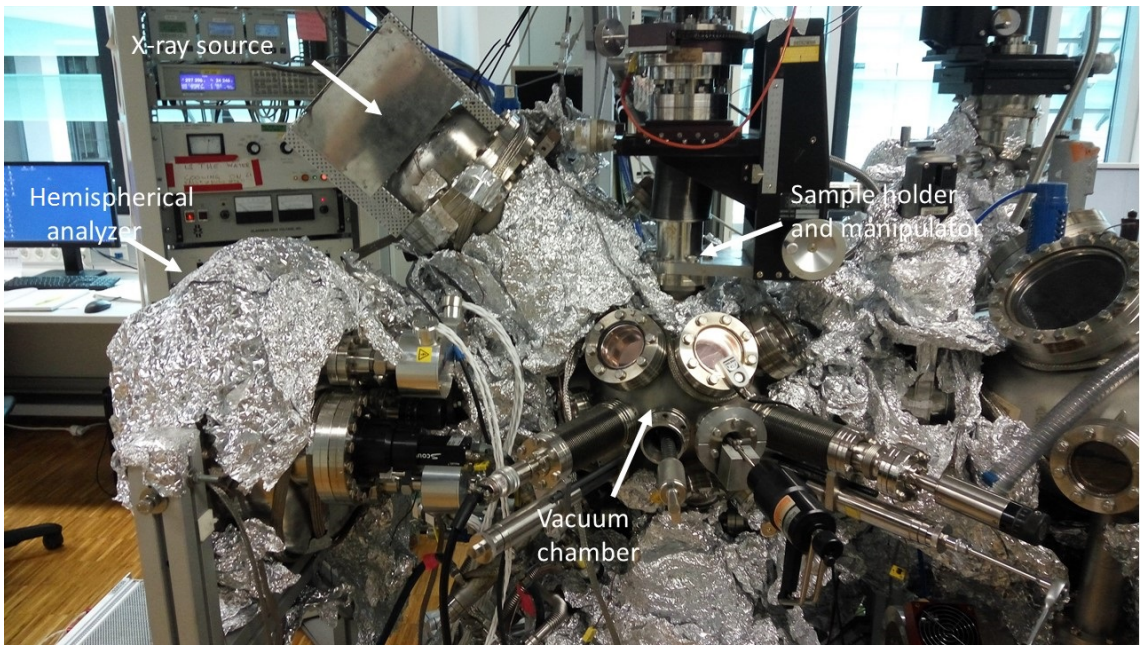

Figure 4.13: XPS facilty at MPI-CPfS in Dresden

4.2.2 EuO stoichiometry

Almost every sample was analyzed with the XPS after the EuO deposition to check the chemical quality of EuO film before growing the Mg, MgO and Cr layers. To perform the analysis, the samples need to be moved immediately after the growth into a dedicated chamber clean from the oxygen used for the growth. The whole transfer is done without breaking the vacuum chain through the use of auxiliary chambers. The first samples, when the growth recipe was not yet optimized, were prepared with recipes taken from literature [43]. It is known that after a threshold oxygen pressures the overoxidation of europium causes the formation of Eu_2O_3 and Eu_3O_4; this is easily detectable with an XPS analysis by the presence of specific features in the spectrum, in different energy regions. In particular, the clearest evidence of the presence of Eu^{3+} in a sample is the shift, of about 10 eV, of the Eu $4d$ peaks, and the appearence of the peak due to the electron removal $4f^6 \rightarrow 4f^5$ at $E_B \approx 8$ eV. For pure EuO, indeed, only the transition $4f^7 \rightarrow 4f^6$ is present at $E_B = 1.9$ eV [47] (see electronic structure in chapter 1).
We first prepared two samples using different oxygen pressures, and we collected 4 different spectra selected energy regions. In particular:

i) O $1s$ peak, at $E_B \approx 530$ eV in europium compounds [48]. This sharp peak in a well defined position is useful to check whether the XPS analysis is affected by charging effect, and if so, to correct the measurements.

ii) Eu $4d$ peaks, in the range $E_B = 180 - 100$ eV [5]. These peaks, at $E_B \approx 140$ eV, show a spin-orbit splitting $\Delta E_{S-O} \approx 6$ eV, with a theoretical *branching ratio* $3 : 2$ in both EuO and Eu_2O_3, but in Eu_2O_3 are shifted to higher E_B of about 10 eV. For some analysis (see par. 4.2.3), we scanned a larger region ($E_B = 180 - 40$ eV) to include also Mg and MgO specific features.

iii) Valence band region, in a range ($E_B = 30 - 0$ eV). This region is important because of the presence of the $4f^6 \rightarrow 4f^5$ and $4f^7 \rightarrow 4f^6$ transitions, that are specific of the Eu_{3+} containing compounds Eu_2O_3 or Eu_3O_4 and EuO respectively. Moreover, if in the sample there is an excess of europium metal, we would see non-zero density of states around the Fermi energy, at $E_B \approx 0$ eV. For pure insulating EuO, there are no states at the Fermi energy.

iv) A very wide scan (VWS), in the range $E_B = 1200 - 0$ eV, was taken in order to have an overview of the whole spectra and to compare it with the reference literature. In particular cases (cf. par. 4.2.3), this spectra would include most of the peaks due to the substrate or the Mg/MgO layers, so it can provide some useful informations about the growth process.

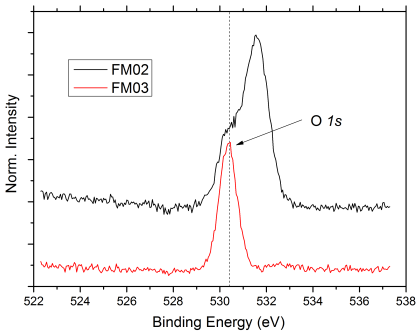

(a) O 1s region

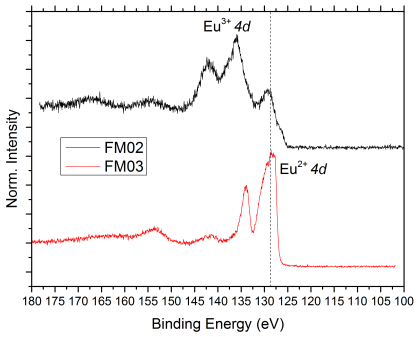

(b) Eu 4d region

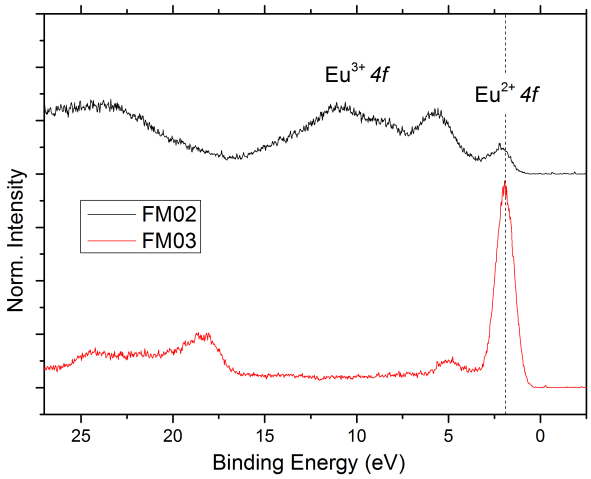

(c) Valence band region

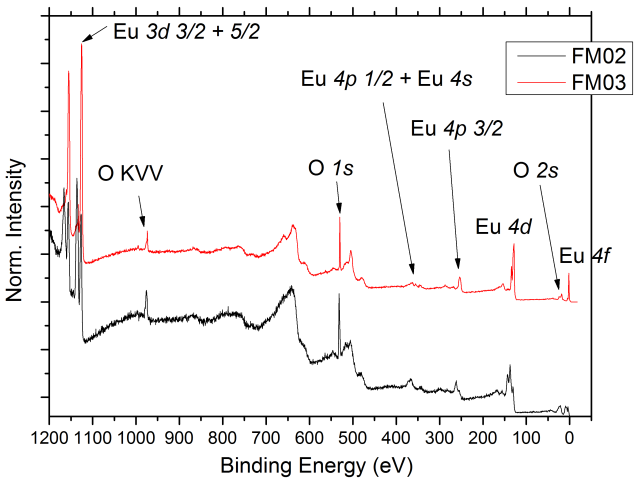

(d) VWS- Very Wide Scan

Figure 4.14: XPS spectra of test samples FM02 and FM03

Fig. 4.14 shows the results of the two samples, FM02 and FM03 grown at oxygen pressure of $5 \cdot 10^{-8}$ and $3.5 \cdot 10^{-8}$ respectively (see table 4.2), for the 4 regions. Before comparing these data with the ones of the next samples, few considerations must be done. As we can see in the plot 4.14(a), O $1s$ peak of FM02 looks quite broad, and a closer inspection shows that it is indeed an overlap of two sharp peaks at slightly different energies. The presence of both peaks indicates a non perfect stoichiometry of the FM02 sample, with the presence of a mixture of EuO and Eu^{3+} species. O $1s$, in EuO, is at a binding energy $E_B \approx 530$ eV, but peak of Eu^{3+} species is shifted towards higher binding energy. This is due to the different chemical environment and the different oxidation state of the oxygen ion, and it is knows as *chemical shift* [45]. The presence of both species is confirmed also by the plot in fig. 4.14(b), where, the presence of both chemical species is clear from the attenuated Eu $4d$ peak of EuO at 129 eV. The Eu $4f$ peak in sample FM03 is in the correct position at $E_B = 1.9$ eV for FM03, but it is highly attenuated in FM02 spectrum (see fig. 4.14(c)).No Fermi edge is visibile for both samples. The very wide scan acquisition gives us an overview of the features over the whole spectrum for the two samples, and by comparison with the reference spectra of europium and oxygen is possible to check the positions of the different peaks. The growth recipe during the first stages of the project was not well defined; indeed, one of the challenges of the project has been to optimize the recipe for the preparation of samples for further analysis. In this perspective, the analysis of the spectra of FM03 shows a good stoichiometry and no presence of formation of Eu^{3+}, so we decided to use them as a reference example of good stoichiometry, and the spectra of FM02 as a reference for a non perfect growth. After this first test, we decided to further narrow down the threshold limit for the oxygen pressure to be used in the growth process. Fig. 4.15 shows the spectra of FMA05, grown with $P_{O_2} = 3.8 \cdot 10^{-8}$ mbar; also for this sample, the mixture of EuO and a small amount of Eu^{3+} is evident. This appeared already in the VWS spectrum, of which is reported a zoom of the region 550-0 eV. Here, both the distinctive marks of Eu^{3+} are visibile, and a more accurate scan of the valence band region clearly shows the presence of overoxidized europium. From these analysis, we concluded that the best

sample	EuO		thickness
	T(°C)	P_{O_2}(mbar)	
FM02	567	$5 \cdot 10^{-8}$	15 nm
FM03	560	$3.5 \cdot 10^{-8}$	15 nm
FM05	561.5	$3.8 \cdot 10^{-8}$	33 nm

Table 4.2: recipe for the growth of the three samples FM02, FM03 and FMA05

recipe was the one used for the growth of the test sample FM03, and we decided to stick to that one for all the following sample. Some results are shown in fig. 4.16.

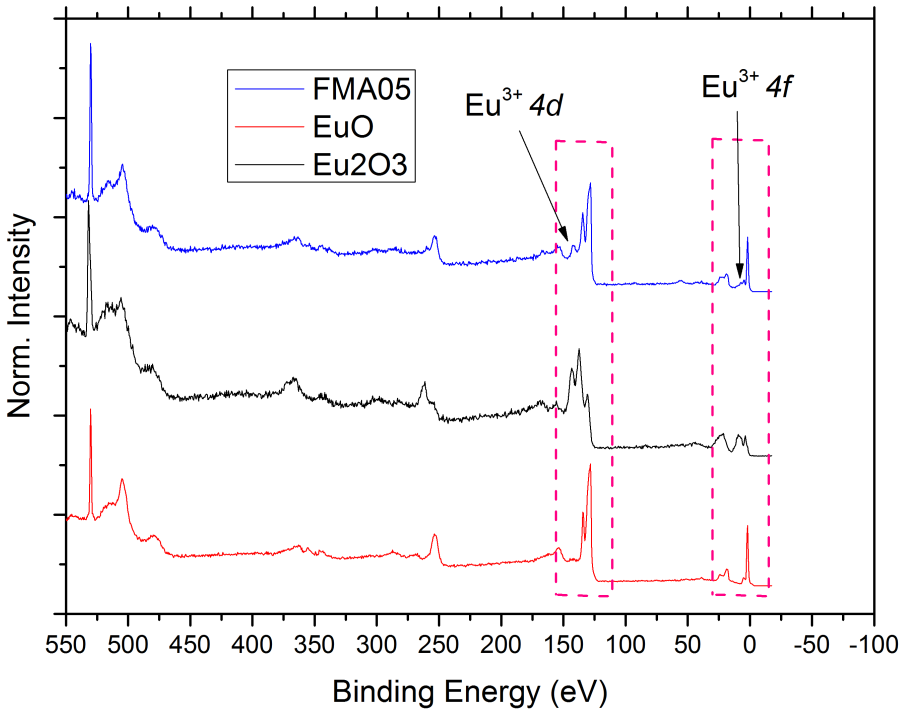

(a) VWS zoom

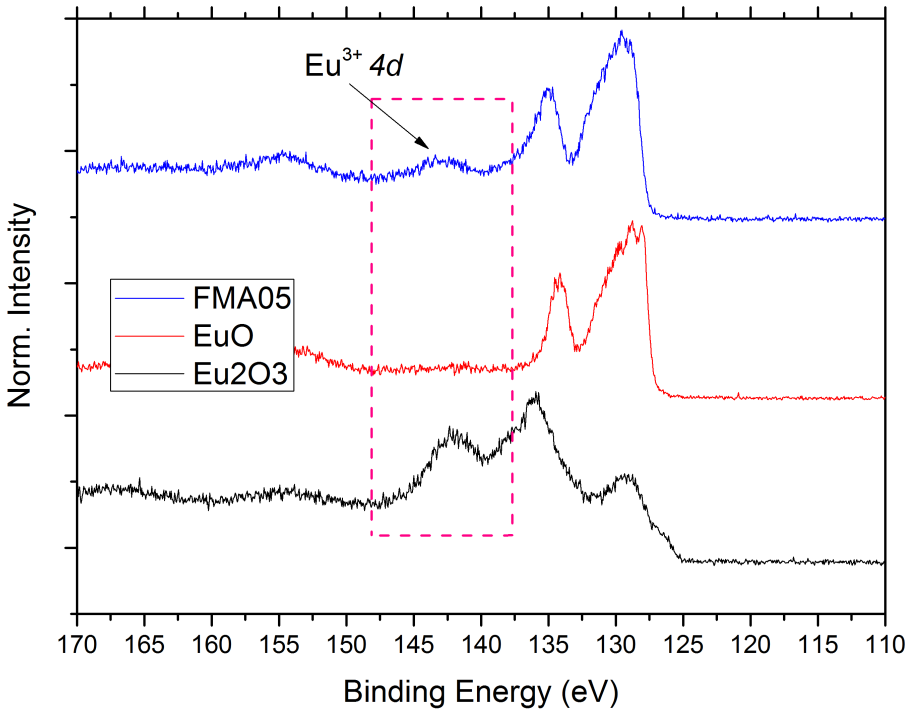

(b) Eu $4d$ region

Figure 4.15: XPS spectra of FMA05 sample, showing the degradation effects due to an excessive oxygen pressure during the growth

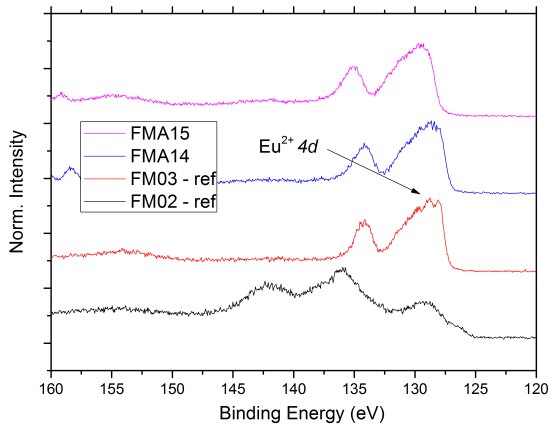

(a) Eu $4d$ region

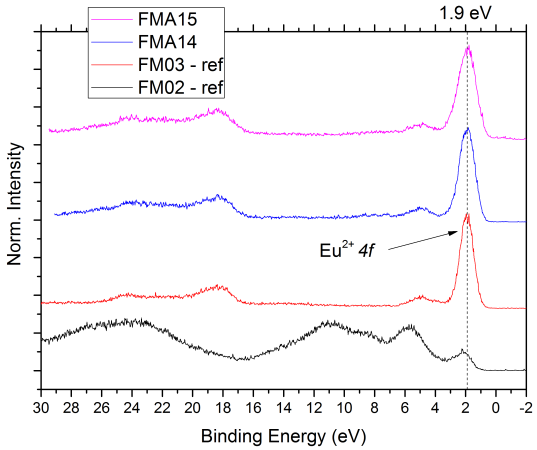

(b) Valence band region

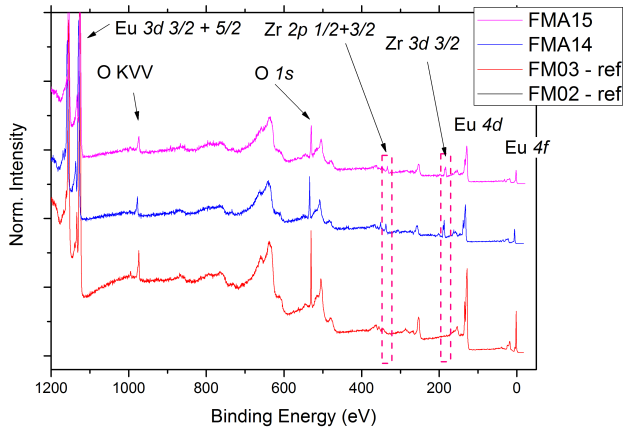

(c) VWS - Very Wide Scan

Figure 4.16: XPS spectra of samples FMA14, FMA15, grown with the corrected recipe and used for magnetic measurements

4.2.3 Mg and MgO growth

The growth of a layer of metal on top of a layer of EuO has been reported many times in literature for different metals. Examples can be found for Au [47], V [49], Al[50][5] and Cr [13]. Provided that the growth process happens at $T_s \approx T_{room}$ there is no re-evaporation of Eu metal, and also from the structural point of view no significant changes has ever been observed in literature. The main risk, in this process, is that the magnesium metal reacts with the sensitive EuO layer, so a dedicated experiment must be performed in order to exclude this possibility. Also the growth of an oxide material like MgO on top of EuO is a difficult challenge, and up to now MgO was used in research about EuO only as a substrate material [51]. The difficulties, for this kind of deposition, come from the high reactivity of EuO surface with the oxygen needed for the growth of MgO. In order to define the succesful recipe described in Chapter 3, we decided to analyze via XPS, on the same sample, the growth of EuO and the successive growth of MgO on top of it. The reference samples for EuO were described in the previous paragraph. Now, we needed a pure MgO samples for reference. Since in this project we were not interested in achieving a good crystal structure of Mg and MgO, we just grew a reference sample directly on YSZ substrates according to the recipe described in the previous chapter, and we analyzed it via XPS. As shown in fig. 3.8, the MgO layer in the sample layout is about 20 nm thick. Such a thickness would prevent all the electrons photogenerated in the EuO layer to escape the surface and reach the analyzer, and as a result a pure MgO layer and a EuO/MgO heterostructure would be undistinguishable. To overcome this problem, we had to grow a very thin layer of MgO ($\approx$ 5 nm) on top of EuO, in order to be able to observe both the MgO and the EuO peaks. Of course, the EuO peaks would be highly attenuated with respect to the usual measurements. Fig. 4.17(a) shows a VWS spectrum in comparison to the reference MgO sample, and the two VWS spectra of the trial sample FM11 after EuO deposition and after EuO/MgO deposition. The pink frames highlight some of the typical EuO oxide features, attenuated in the film covered with MgO (blue curve). Fig. 4.17(b) shows the spectrum of the Eu $4d$ region, where both the Mg $2s$, $2p$ peaks and the Eu $4d$ peak are visible. No satellite features, are visible in the spectrum of the EuO/MgO sample, giving another clear indication that all the magnesium metal has been oxidized to form magnesium oxide (MgO). The presence of magnesium metal, indeed, could have been detected by the presence of plasmon peaks typical of XPS experiments on metals. Since no signs of the presence of Eu^{3+} compounds are visible, we could conclude that the MgO deposition process described in Chapter 3 was succesful and could be used for the preparation of the successive samples.

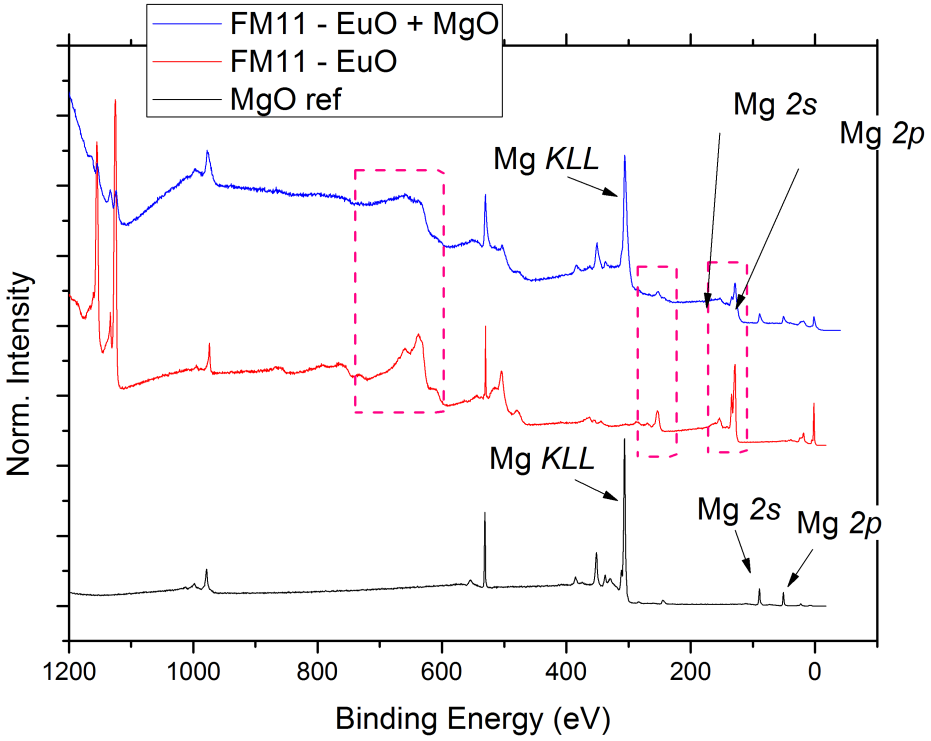

(a) VWS - Very Wide Scan

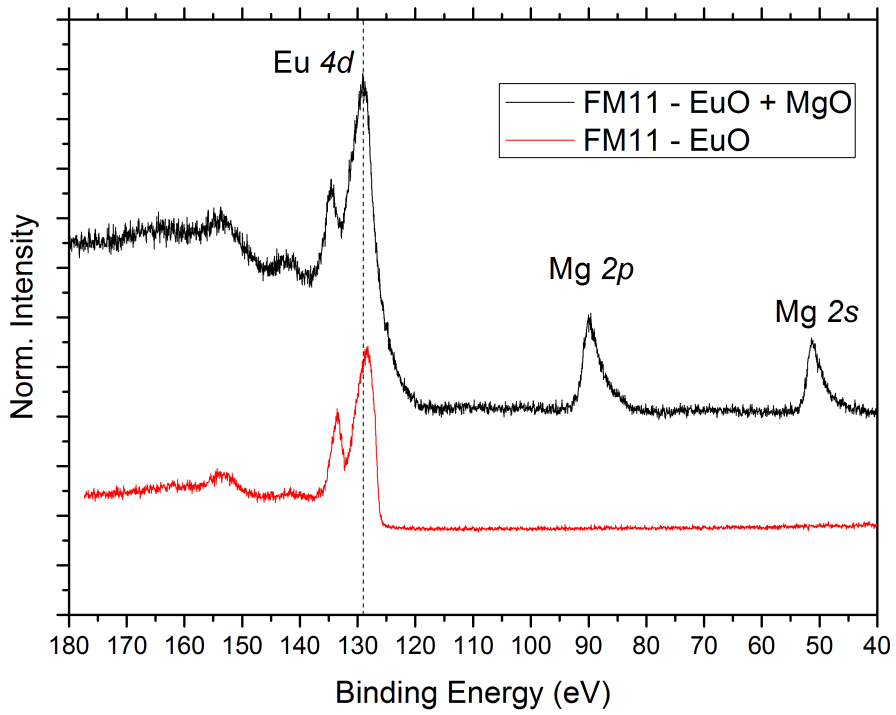

(b) Eu $4d$ region

Figure 4.17: Spectra of test samples used to check the growth of MgO on EuO

4.3 Hard X-Ray Photoelectron Spectroscopy - HAXPES

4.3.1 Motivation and experimental setup

As reported in chapter 4.2, surface stoichiometry and chemical composition can be effectively checked with XPS, without the need to extract the sample from the vacuum environment and to expose it to atmospheric condition and contaminations. To grasp informations about the bulk composition and to do more sophisticated analysis, however, a simple in-house XPS facility is not always sufficient. The most advanced and reliable X-ray photoemission studies, indeed, are performed using *synchrotron radiation*.

Instead of using a the radiation emitted by a specific electronic transition of an element (Al, Mg) as a source of X-rays, synchrotron radiation is generated by electrically charged particles (electrons, in particular), focused in a beam and accelerated at relativistic speed along a circular ring. The principle for which an accelerated particle produces electromagnetic radiation has already been described for non-relativistic speed by Larmor in the end of 19th century, and it was later generalized by Liénard for the case of curved trajectories [52]. But the most interesting properties of the synchrotron radiation comes mainly from the relativistic speed to which electrons are accelerated, so a relativistic analysis is needed for a quantitative description.

For our purpose, it is enough to list the principal characteristics of the synchrotron radiation, and their benefits with respect to Al-$K\alpha$ radiation of the *in-house* XPS device.

i) High brilliance and low divergence; for nanometric structures, as the one used in this project, it is fundamental to have high intensity photon beams confined in a restricted area.

ii) Continuous spectral distribution; the possibility of having a continuous range of incident wavelength allows to perform a huge amount of different experiments. In particular, we performed a similar analysis with respect to XPS, but using a 6.5 keV incident photon beam.

iii) Polarization of the beam; emitted photons have a specific angular moment, that can couple with the spin or the orbital angular moment of the electrons in the sample. This feature is not used in an HAXPES experiment, but can be exploited for the characterization of magnetic materials.

The HAXPES principle is the same of XPS, but with different photon energies (in our case, 6.5 keV): light-generated electrons are emitted from the sample and detected by the analyzer, and from their kinetic energy it is possible to determine the energy scale of electrons in the solid. The higher photon energy enables to investigate deeper (in energy) core levels with respect to XPS, such as the n=3 shell of Eu with a good resolution of all the subshells $3s$, $3p$, $3d$. The experiments

were performed at the NSRRC-BL12XU beamline at the SPring-8 synchrotron radiation facilty in Hyogo Prefecture, Japan. The endstation is equipped with two MBS hemispherical analyzers, and is shown in fig. 4.18. We used an horizontal geometric configuration between the sample and the analyzer. In this configuration, the X-ray beam impinges onto the surface at grazing angle of about 3°. A simpler sample layout was designed for HAXPES experiments (and XRR, see paragraph

Figure 4.18: endstation of BL12XU beamline, in Spring8

4.4), and is shown in fig. 4.19. The purpose of the experiment was both for the present and future

Figure 4.19: Layout of the samples analyzed during HAXPES experiments

research: First of all, we wanted to check the bulk composition of the sample, not accessible with XPS analysis. Moreover, we wanted to check the reliability of the Cr capping in terms of protection of the sample from degradation. This is useful because samples must be extracted from the vacuum chamber in order to perform magnetic analysis (see chapter 5), and Cr capping must be effective in preserving EuO quality. Also, further studies are going to be performed on similar samples, and

transportation from the preparation laboratory to the synchrotron facility might affect the samples quality. With a normal XPS, such an analysis could not have been performed, because the Cr capping is too thick to enable electrons to be photogenerated in the Eu layer and to be detected by the analyzer. The drawback of such an experiment is that also the energy levels or Cr metal are present in the spectrum, and in some cases they might dominate the whole spectrum.

We decided to grow a thicker EuO layer (≈ 40 nm) and a chromium layer of the usual thickness (10 nm) to check its reliability as a capping layer. There was no need for the Mg and MgO layer, since we have already checked that their growth does not affect the underlying EuO layer. Samples were grown in Dresden, in the usual MBE facility, and conserved during the transportation under static vacuum in a specially designed vacuum suitcase. The shipping took some days, and once there the vacuum suitcase was directly mounted in the endstation and the samples were analyzed. The first

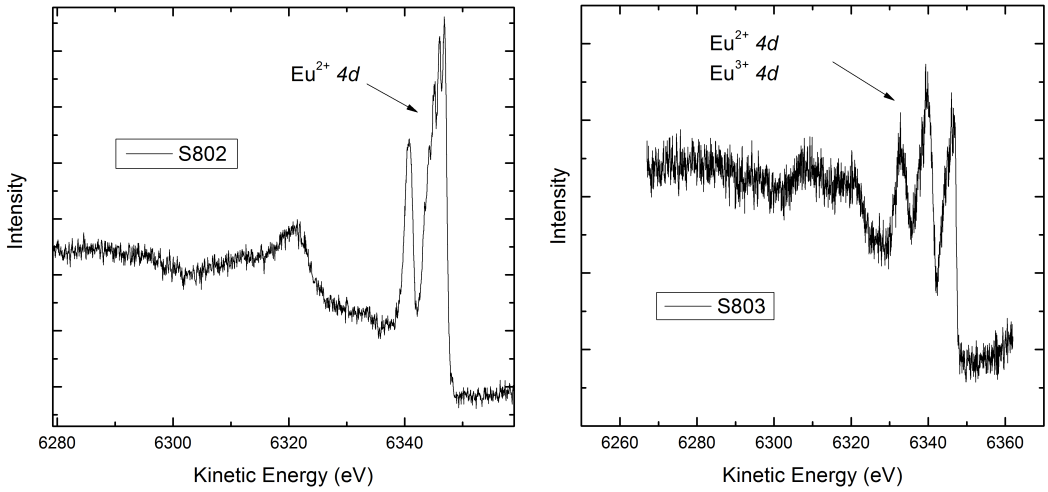

Figure 4.20: HAXPES spectra of the $4d$ region for the two samples S802 and S802

sample, S802, shows a good stoichiometry and no contaminations nor Eu^{3+} formation. Fig. 4.20 shows indeed the usual Eu $4d$ feature typical of EuO. Here, this analysis is crucial, because as is shown in fig. 4.21 the valence band is dominated by the presence of chromium, as is to be expected for metals, and there is no possibility to check the exact position and the shape of the Eu $4f$ peak. Chromium features are dominant also in the spectrum reported in fig. 4.21, where the intensity of the core peaks of Cr $2s$ and Cr $2p$ can be compared with the O $1s$ peak. In XPS analysis of pure EuO, the same O $1s$ peak was one of the most intense and visible, so much that we used it as a reference to monitor and correct eventual shift due to charging effect. In fig. 4.22 the Eu $3d$ peaks are shown, superimposed on the background noise. Sample S803, however, displays a large amount ofEu^{3+}, as shown in fig. 4.20. No further analysis have been done on this sample, because it was already clear that something went wrong during the transportation from the laboratory to the synchrotron facility. It is highly probable that the vacuum suitcase designed to protect the samples

from atmospheric environment and to prevent degradation effects was not as effective as expected. In fact, all the samples shipped to Spring-8 have been also checked directly after the growth with the XPS, and none of them showed presence of Eu^{3+}. Because of this, a new vacuum suitcase is now being designed and will be tested. If the results will be satisfactory, it will become the standard shipping method for sensitive samples for future experiments.

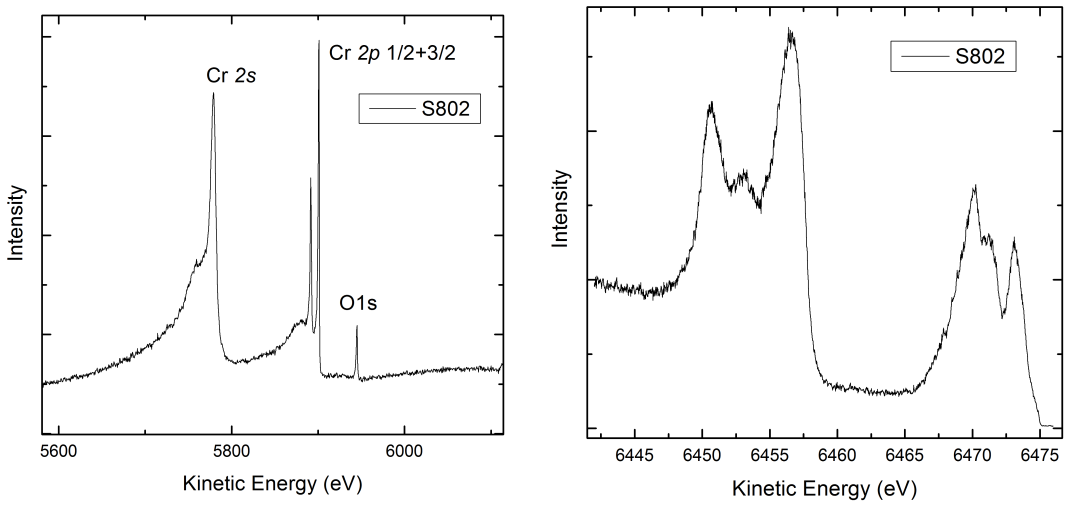

Figure 4.21: HAXPES spectra of the Cr features and valence band region, for S802

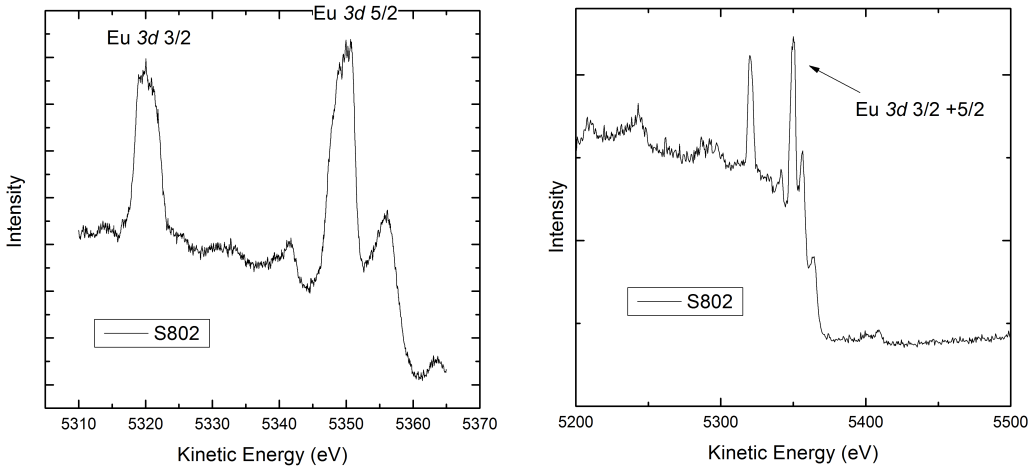

Figure 4.22: HAXPES spectra of $3d$ region, for S802

4.4 X-Ray Reflectivity - XRR

4.4.1 Theoretical introduction and motivations

X-Ray Reflectivity (XRR) is a technique routinely used to characterize surfaces, thin films and layered heterostructures. In this project, we used it to gain informations about the sample thickness, in order to compare the results obtained by XRR with the estimations based on RHEED oscillations and with the nominal thickness based on the growth time as determined by the quartz crystal microbalance. The general theory of the reflection of X-rays from surfaces and thin films is complicated, and accounts for the wide range of informations (thickness, density, surface roughness, crystal quality) provided by an X-ray experiment. A complete description can be found in M. Birkholz et al. [53]. For our purpose, however, a simple discussion is sufficient, such as the one in an article by Yakasa [54] that will be summarized here. As well known from elementary optics, electromagnetic waves incident onto a sample can be reflected or refracted from the surface according to refractive index n of the material. In the case of X-rays, and in particular for the Cu-$K\alpha$ radiation commonly used in XRD devices, the refractive index of materials is generally slightly less than 1. Therefore, it is possible to define a so-called critical angle for total reflection (θ_C), for which the X-rays undergo a total reflection when incident on a flat surface of a material at a grazing angle smaller than (θ_C); fig. 4.23 explains this concept visually.
During a 2θ experiment, the incident angle is slightly changed and the intensity of the reflected X-rays is recorded and plotted on a logarithmic scale. The choice of a logarithmic plot is due to the wide dynamic range of the recorded intensity. When a layered structure of different materials is analyzed, like the one in fig 4.19, different densities and different refractive indexes are experienced by X-rays. There are then reflections and refractions at every interface between different materials. Changes in the recorded intensity happen due to the interference between the X-rays reflected at every interface, in this case YSZ/EuO and EuO/Cr, and Cr/air. The typical reflectivity curve shows oscillations, called *Kiessig fringes*, due to this interference. In particular, the thicker the film, the shorter the period of the oscillations. By measuring the angular period of these fringes, it is possible to have a good approximation of the thickness of the layer analyzed, by using the formula.

$$d \approx \frac{\lambda}{2 * \Delta\theta(\text{rad})} \tag{4.7}$$

Here, $\Delta\theta$ is the difference between two consecutive maxima of the 2θ reflectivity curve, and λ is the wavelength of the X-rays used for the analysis. The measurements were carried out using a Philips X'Pert MRD diffractometer that uses a Cu-$K\alpha 1$ radiation with a wavelength of 1.54 Å. The main drawback of XRR is that in general it is impossible to perform it *in-situ*, and this could

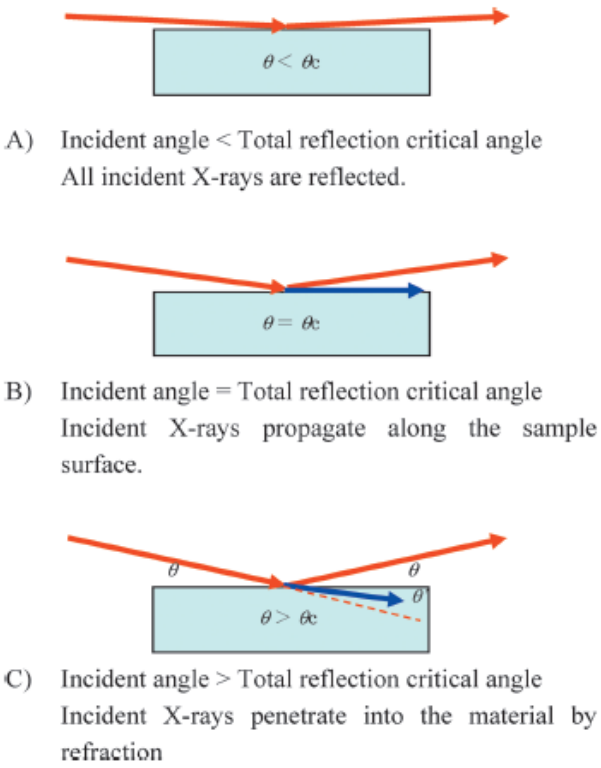

Figure 4.23: Schematics of reflection and refraction of X-rays. From [54].

be a decisive factor for sensitive samples as the ones of this project.

4.4.2 Results

In order to perform a XRR analysis, we grew several samples with the layout in fig. 4.19, and we compared the nominal thickness calculated with the period of the RHEED oscillations with the XRR results. For the sample analyzed, FMA04, RHEED showed a good crystalline quality, and the calculation based on RHEED oscillations analysis predicted a theoretical thickness:

$$\text{thickness (Å)} = \frac{a\ (\text{Å})}{2 * T_{osc}} * \text{time (s)} \approx 462.9\ \text{Å}. \tag{4.8}$$

Fig. 4.24 shows the reflectivity curve for the FMA04 sample. The angular period is $\Delta\theta = 0.19°$, so the calculated thickness would be

$$d \approx \frac{\lambda}{2 * \Delta\theta(\text{rad})} \approx 464\ \text{Å} \tag{4.9}$$

in almost perfect agreement with the RHEED estimation. This confirms the validity of our hypothesis about thickness of the samples, and enabled us to proceed with the work without the need of further *ex-situ* XRR analysis.

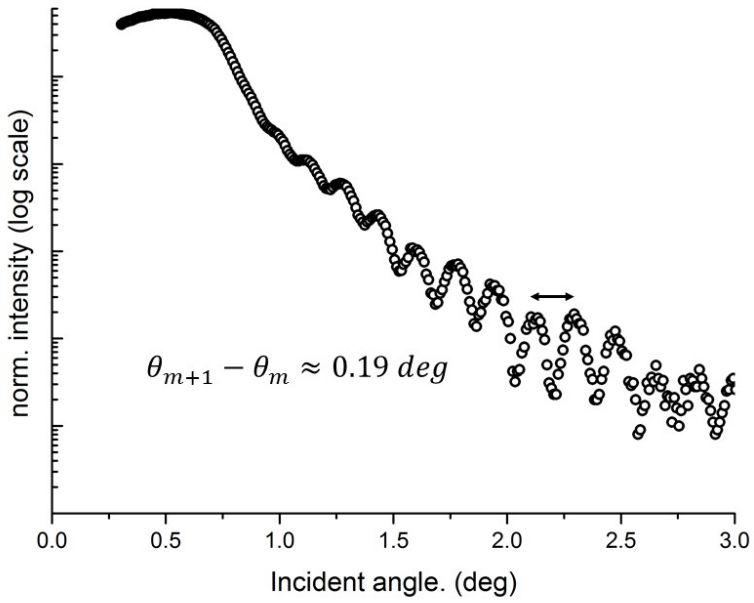

Figure 4.24: Interference curve of the XRR experiment on YSZ/EuO/Cr

5. Magnetic measurements

5.1 Superconductive Quantum Interference Device - SQUID

5.1.1 Magnetic flux quantization

The instrument used for the magnetic characterization of the samples is called Magnetic Properties Measurement System, and it is based on a Superconducting Quantum Interference Device (SQUID). Such a device uses the properties of electron-pair wave coherence inside a superconductor, and a Josephson junction to detect very small magnetic fields. A short theoretical background is needed to understand the working principle and the results obtained. Superconductors are a large class of material that exhibits a diversity of exotic properties, among which a resistanceless current flow below a certain critical temperature. An exhaustive theory for the physics of superconductors has yet to be developed. Up to now, one of the most successful attempt to explain superconductivity is the so-called BCS theory, after the names of the scientists who proposed it in 1956 [55]. According to BCS theory, at sufficiently low temperatures, the electrons near the Fermi level become unstable against the formation of electron-electron pairs, the so called *Cooper pairs*. In conventional superconductors, the attractive potential is phonon-mediated: lattice deformations cause local increase of positive charge that screens the electron-electron Coulomb repulsion.
Coopers pair are a *composite boson* with $S = 0$ or $S = 1$ and charge $2e$, and the resistanceless current flow is a macroscopic effect of the condensation, below a certain temperature, of Cooper pairs in a large Bose-Einstein condensate. Because of this, the pairs wavefunctions are coherent over a very long distance, and we can treat the boson probability amplitude $\psi(\mathbf{r})$ as a classical quantity. A complete discussion of this topic can be found in almost every physics textbook, at different level of complexity; the one proposed here is a slightly modified version of the discussion present in [56]. If we suppose that the pair concentration $n = \langle\psi|\psi\rangle$ is constant, we can write

$$|\psi(\mathbf{r})\rangle = n^{\frac{1}{2}} e^{i\theta(\mathbf{r})} \quad \langle\psi(\mathbf{r})| = n^{\frac{1}{2}} e^{-i\theta(\mathbf{r})} \tag{5.1}$$

where $\theta(\mathbf{r})$ is the space phase of the wavefunction. The general expression for the velocity of a charged particle ($q = 2e$) in presence of a magnetic field can be directly derived from the Hamiltonian

$$\mathbf{v} = \frac{1}{m}(\mathbf{p} - 2e\mathbf{A}) = \frac{1}{m}(-i\hbar\nabla - 2e\mathbf{A}) \tag{5.2}$$

The particle flux ϕ and the current density J_s are then:

$$\phi = \langle\psi|\mathbf{v}|\psi\rangle = \frac{n}{m}\left(\hbar\nabla\theta - 2e\mathbf{A}\right) \tag{5.3}$$

$$J_s = 2e\phi = \frac{2en}{m}\left(\hbar\nabla\theta - 2e\mathbf{A}\right) \tag{5.4}$$

When a current flows along a path γ on a superconductor, without any resistance, there will be a time-constant phase difference between the endpoint of the path. In particular, since the probability amplitude is a measurable quantity in the classical approximation, it must be single valued and if we consider any closed path γ, the phase difference must respect

$$\Delta\theta = \oint_\gamma \nabla\theta \cdot d\mathbf{l} = 2\pi s \tag{5.5}$$

where s is an integer. Moreover, for a superconductor both B and J are null in the interior because of the Meissner effect. This means that eq. 5.4 must be zero, and:

$$\hbar\nabla\theta = 2e\mathbf{A}. \tag{5.6}$$

We can apply the Stokes theorem, and obtain the magnetic flux Φ as:

$$\oint_\gamma \mathbf{A} \cdot d\mathbf{l} = \iint_S \nabla \times \mathbf{A} \cdot d\sigma = \iint_S \mathbf{B} \cdot d\sigma \equiv \Phi_B. \tag{5.7}$$

By joining eq. 5.5, 5.6 and 5.7, we get:

$$\Phi = \oint_\gamma \mathbf{A} \cdot d\mathbf{l} = \frac{\hbar}{2e}\oint_\gamma \nabla\theta \cdot d\mathbf{l} = s\frac{h}{2e} = n\Phi_0. \tag{5.8}$$

This relation shows that the magnetic flux is quantized, and can have only values that are discrete multiples of the quantity Φ_0, the quantum of magnetic flux equal to $2.07 \cdot 10^{-15}$ Wb. When an external source of magnetic field, like a ferromagnetic sample, is inserted in the ring, the total flux throught the ring will be the sum $\Phi = \Phi_{ext} + \Phi_{current}$. Usually, the external flux is not quantized, and the quantization condition holds for the whole flux Φ; the flux due to the supercurrent $\Phi_{current}$ must adjust itself in order to fulfill this condition, and it is this adjustment that is detected by the SQUID.

5.1.2 Josephson Junction and DC Josephson Effect

Like with electrons, also Cooper pairs are subject to quantum tunneling. In particular, when two superconducting regions are brought close enough to the other, electron-pairs will be able to tunnel across the gap, even in absence of any applied voltage, and the two electron-pair waves will become coupled. As the separation decreases, the tunnelling will be more effective, and the the strength of the coupling increases. In real Josephson juctions, the separation is achieved by a thin

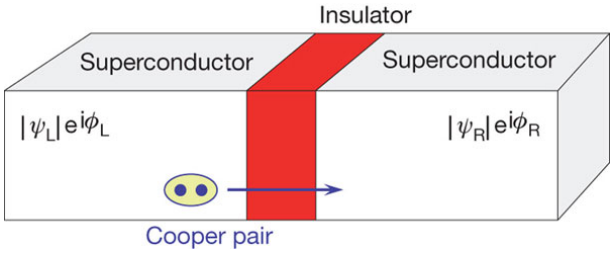

Figure 5.1: Pictorial representation of the Josephson effect. Picture from [57].

layer of insulating or non superconductive material. In fig. 5.1 is depicted a schematic of this phenomenon. A simple description of this phenomenon is based on the application of the time-dependent Schrödinger equation to the Cooper pairs in the two regions, whose wavefunction is of the form of eq. 5.1. Assuming that $|\psi_L\rangle$ is the wavefunction in the left region, and $|\psi_R\rangle$ the one in the right region, then we can write

$$i\hbar\frac{\partial|\psi_L\rangle}{\partial t} = \hbar T|\psi_R\rangle \quad i\hbar\frac{\partial|\psi_R\rangle}{\partial t} = \hbar T|\psi_L\rangle \tag{5.9}$$

where T is a rate, or frequency, and $\hbar T$ represents the effect of the electron-pair coupling, or the transfer across the insulator. By calculating the time derivative of the densities $n_L = \langle\psi_L|\psi_L\rangle$ and $n_R = \langle\psi_R|\psi_R\rangle$, it is possibile to derive and expression for the current density J across the junction of the form

$$J = J_C \sin(\theta_R - \theta_L) \tag{5.10}$$

where J_C, the *critical current*, is the maximum current that can pass throught without causing a voltage drop across the junction, and it is dependent on the transfer interaction T.

5.1.3 DC-SQUID magnetometer

The direct current superconducting quantum interference device (dc SQUID) consists of two Josephson junctions connected in parallel. The central element of a SQUID magnetometer is thus a ring of superconducting material with two weak links (see fig. 5.2).

Because of this weak coupling, the typical current across the junctions is much smaller than the critical current in a single superconducting specimen. This produces a very low current density making the momentum of the electron pairs small. Consequently, the wavelength of the electron-pairs is very long, leading to little difference in phase between any parts of the ring. In presence of a magnetic field B_{ext}, perpendicular to the plane of the ring, a phase difference is produced between the electron-pair waves in the two parts of superconductor separated by the non-superconducting junctions, as clear from the relation 5.10. The hase difference, and the total flux as a consequence, are quantized, as stated in equation 5.5. In order to fulfill the quantization relation a small current

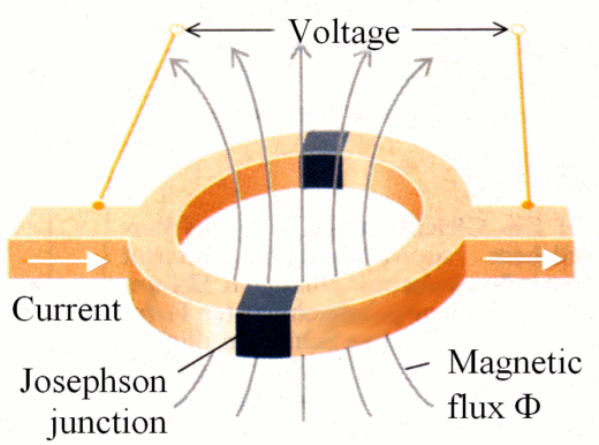

Figure 5.2: Schematic representation of a SQUID ring. Picture from [58].

is induced in the ring, that can be both in the same or in the opposite direction of the field-induced one. It is energetically favorable to induce an opposite current, so that the magnetic energy density in the ring is reduced. The magnitude of this small induced current density is:

$$J = J_C \sin(2\pi \frac{\Phi_{ext}}{\Phi_0}). \tag{5.11}$$

The current circulating in the ring is then periodically dependent of the flux of the applied magnetic field Φ_{ext}, and so from its magnitude, with a period Φ_0. Detecting this circulating current enables the use of a SQUID as detector of small magnetic fields. The SQUID device thus functions as a transducer for magnetic flux, producing measurable voltage changes at its output for small changes in magnetic flux applied at the input.

5.1.4 Magnetic Property Measure System - MPMS

All the magnetic measurements presented in this thesis were obtained using a SQUID-based device called Magnetic Property Measure System (MPMS). A typical MPMS system can be ideally divided in two main parts: the probe, dewar and SQUID assembly, that acquire the signal, and the electronic control system that elaborates the signal. The probe contains a high precision temperature control system, allowing measurements between 2 and 400 K, with an accuracy of 0.01 K, and a superconducting electromagnet giving a field up to 5 T. The dewar consists of an inner liquid helium reservoir, needed both for maintaining the electromagnet in a superconducting state and for cooling the sample below the Curie, or Néel, temperature. Samples are mounted within a clear plastic straw that has a minimal magnetic susceptibility. The straw is connected to one end of a rod which is inserted into the dewar. The end of the rod is attached to a motor which is used to position the sample within the center of the SQUID pick up coils. Two kind of acquisitions are possible: in DC measurements, the sample is moved through the coils in discrete steps, while in RSO

Figure 5.3: MPMS device used for the magnetic measurement characterization of the samples

measurements are performed using a servo motor which lets the straw, and so the sample, rapidly oscillate. A shaft encoder on the servo motor records the position of the sample synchronous with the SQUID signal. The data received are fitted to an ideal dipole moment response. To ensure this

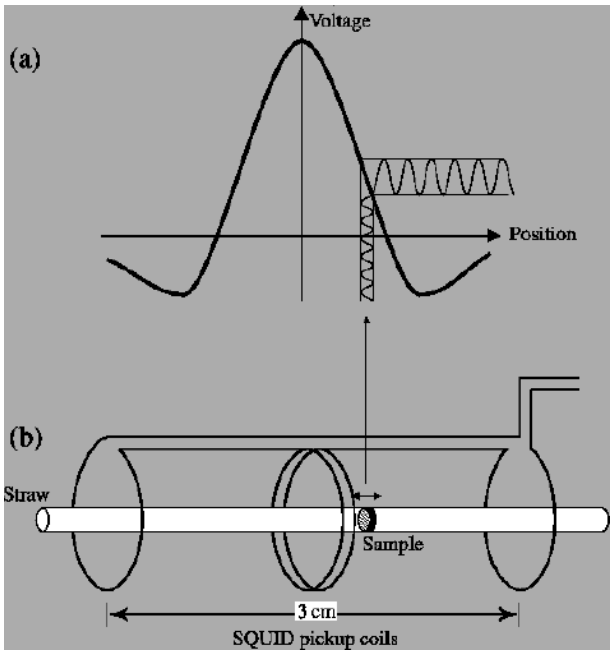

Figure 5.4: Illustration of an RSO measurement with a small amplitude. a) Ideal SQUID response for a dipole. b) Movement of the sample within the pick up coils. Picture taken from [59]

assumption is applicable, samples need to be as small as possible. On the other hands, samples too small would give a low signal, too low to be detected by the device. For this reason the original sample, grown on a $10\times10\times0.5$ mm^3 substrate needed to be cleaved in smaller pieces. A particular care was necessary in handling the sample with tools of non-magnetic materials in order to avoid

contamination of the surface. After the MPMS collects the raw data, it uses an iterative regression

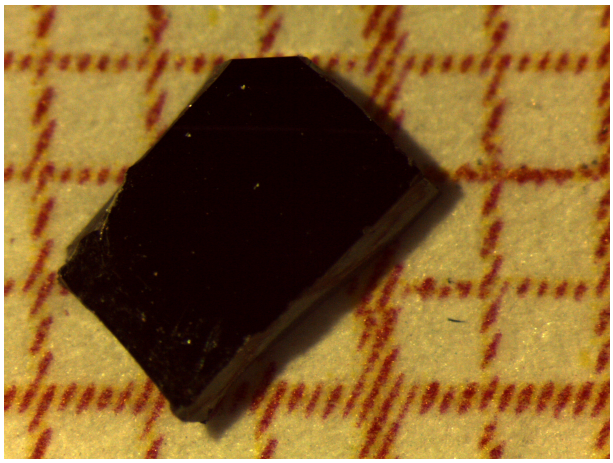

Figure 5.5: Picture of the piece of FMA08 sample analyzed with the MPMS. The image was taken with an optical microscope, and the reference is a 1mm×1mm grid

algorithm to compute the magnetic moment of the sample, by fitting the measurement data with an analytical curve.

5.2 Methods and results

The value of the magnetic moment measured is indeed affected by the substrate contribution. The substrate YSZ and the additional layer of MgO used to prepare the samples are both diamagnetic, so their magnetic contributions should be completely absent in all zero-field measurements, and for non-zero field measurements clearly distinguished in the sample saturation region with respect to the ferromagnetic EuO signal. Chromium use as capping is antiferromagnetic, and its magnetic signal must be compared with the signal of EuO. After a test measurement (fig. 5.6), we showed that Cr contribution to the total magnetic moment is negligible with respect to EuO one. Magnesium metal, despite having two paired electrons in the $3s^2$ subshell, is paramagnetic with a small magnetic susceptibility $\chi_m = 1.2 \cdot 10^{-5}$ [60]. This is due to the interaction between the external magnetic field and the spins of conduction electrons in the Fermi gas, an effect known as *Pauli paramagnetism*. Its magnetic signal is smaller than the one EuO, and superimposed to it. Two main kind of measurements were performed. The first is a magnetization vs. temperature ($M(T)$) measurement, meaning that the sample was kept at a constant external magnetic field of 50 Oe while the temperature was varied from 5K to 300K, and back again, in order to cross the Curie temperature and observe the ferromagnetic ordering of the sample. This are the measurements that provides the information about the Curie temperature. The other one is a magnetization vs. applied field ($M(H)$) measurement. Here, the ferromagnetic order was destroyed by increasing

the temperature above T_C, then a zero-field cooling was performed until $T = 5$ K. An external magnetic field was then applied to the sample, according to the following procedure, in order to perform a whole closed hysteresis loop:

1) $0 \rightarrow 2000$ Oe, measuring every 40 Oe (41 steps)

2) $2000 \rightarrow 5000$ Oe, measuring every 500 Oe (7 steps)

3) $5000 \rightarrow 2000$ Oe, measuring every 500 Oe (7 steps)

4) $2000 \rightarrow -2000$ Oe, measuring every 40 Oe (81 steps)

5) $-2000 \rightarrow -5000$ Oe, measuring every 500 Oe (7 steps)

6) $-5000 \rightarrow -2000$ Oe, measuring every 500 Oe (7 steps)

7) $-2000 \rightarrow 2000$ Oe, measuring every 40 Oe (81 steps)

2) $2000 \rightarrow 5000$ Oe, measuring every 500 Oe (7 steps)

The output of the measurement system is a magnetization value, expressed in EMU (1 EMU $= 10^{-3}$ J/T). The value of the effective magnetic moment (per functional unit) is obtained, in unit of μ_B, with the following relation:

$$M_{eff} = \frac{M_{meas} * V_{cell}}{V_{sample} * FU * \mu_B} \tag{5.12}$$

where M_{meas} is the value measured by the MPSM, V_{sample} is the volume of EuO in the sample, V_{cell} and FU and the number of functional unit of each cell (see chapter 1 for the numeric values) and μ_B is the Bohr magneton. The second measurement is useful to check the magnetic quality of the samples and to monitor a possible presence of degradation effects. For comparisons of the magnetic signal of different materials, a normalization of the results by the area of the sample (A_s) is used:

$$M_{area} = \frac{M_{meas}}{A_{sample}} \tag{5.13}$$

The area of the sample was measured with a commercial software using an optical microscope image and a 1×1 mm grid as a reference. In fig. 5.6 the results of $M(H)$ measurements on samples SA006, SA008 and SA009 are shown, whose layers chemical compositions and thicknesses are reported in tab 5.1.

This confirms the expected behaviour of the various magnetic signals. The blue curve shows the typical hysteresis loop of ferromagnetic EuO, and the superimposed linear diamagnetic behaviour of YSZ substrate. Indeed, the black curve shows a positive linear dependency of the magnetization, whose slope is given by the magnetic susceptibilities of the substrate and of the chromium layer and whose magnitude is negligible with respect to the EuO. The behaviour of the red curve is dictated

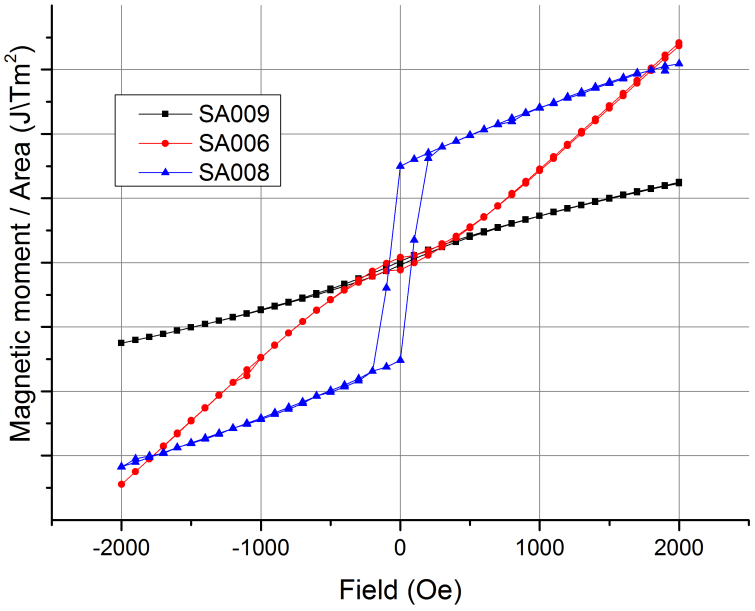

Figure 5.6: Results of M(H) measurements on samples SA006, SA008 and SA009

sample	layer and thickness (Å)				
SA006	YSZ		Mg (200 Å)	MgO (500 Å)	Cr (100 Å)
SA008	YSZ	EuO (25 Å)			Cr (100 Å)
SA009	YSZ				Cr (120 Å)

Table 5.1: composition of the samples SA006, SA008, SA009

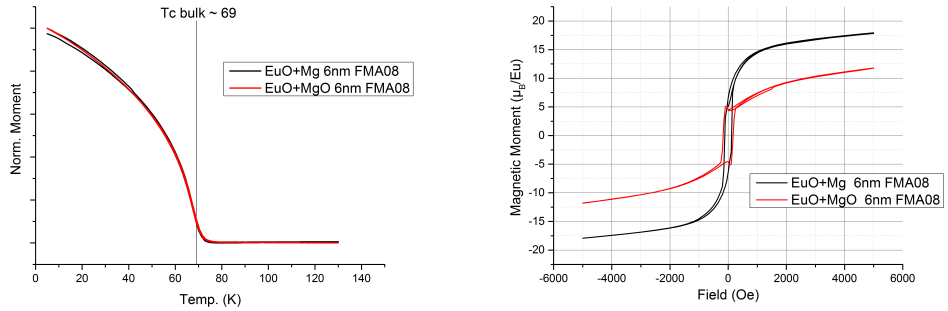

(a) $M(T)$ (b) $M(H)$

Figure 5.7: Results of magnetic measurements of sample FMA08 - EuO, 6nm.

by the complex superposition of diamagnetic MgO and YSZ and paramagnetic Mg. From the figure, it is clear that their signal is negligible with respect to EuO. After proving that the substrate and the successive layers do not compromise further measurements, we started to grow and analyze samples of decreasing EuO thicknesses (cf. tab. 3.1). Each sample was broken in smaller pieces, in order to take one of EuO interfaced with Mg and one of EuO interfaced with MgO. For each of them, a complete magnetic characterization was performed. In order to compare the results with the ones in literature [18], we chose as a measure for T_C the inflection point of $M(T)$ curve. In Fig. 5.7 the result of the two measurements for a 6nm sample, FMA08, is shown (cf. tab 3.1 for the growth conditions). As expected, for t$\approx$ 6 nm no finite size effects are present and we observe a behaviour similar to the bulk one, with $T_C \approx 69$ K. No difference can be observed between the two different capping layers, as shown in the plot on the left in fig. 5.7.

The plot on the right in fig. 5.7 shows two hysteresis loops, with a quite different behaviour and a strong difference in the magnitude. The saturation magnetization of the EuO/Mg sample piece is over $15\mu_B$ per functional unit, well above the expected value of $7\mu_B$. The possible explanation is the presence of some ferromagnetic contaminations, in the substrate or on the sample, that alters the magnetic measurement.

5.2.1 Magnetization vs. Temperature - M(T)

The reduction of Δ and U due to the image charge screening (see eq. 2.17 and 2.15) affects the strenght of the magnetic interactions by increasing the constant J_{ex} and $J_{superex}$ as in eq. 5.14b.

$$J_{ex} = \frac{4t^2}{U} \tag{5.14a}$$

$$J_{superex} = -\frac{4t_{pd}^4}{(U_d + \Delta_{pd})^2}\frac{1}{U_d} + \frac{1}{U_d + \Delta_{pd}} \tag{5.14b}$$

This would result in an increase of the ordering temperature T_C, that would be higher in the samples of EuO interfaced with Mg with respect to the ones with Eu/MgO configuration. In fig. 5.8 the results of the $M(T)$ dependence of four samples, for both the Eu/Mg and the Eu/MgO pieces, are shown. The samples analyzed, namely FMA08, FMA15, FMA14, FMA17, have decreasing EuO thicknesses 6 nm, 3 nm, 2.5 nm and 1.5 nm. From these results the drastic reduction of T_C due to

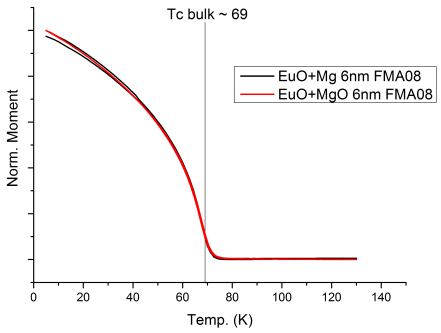

(a) $M(T)$ for FMA08 - 6nm

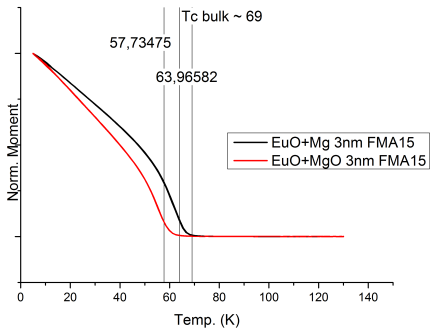

(b) $M(T)$ for FMA15 - 3nm

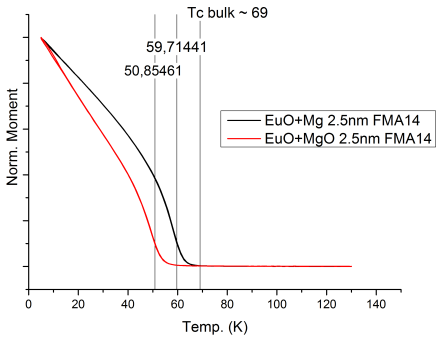

(c) $M(T)$ for FMA14 - 2.5nm

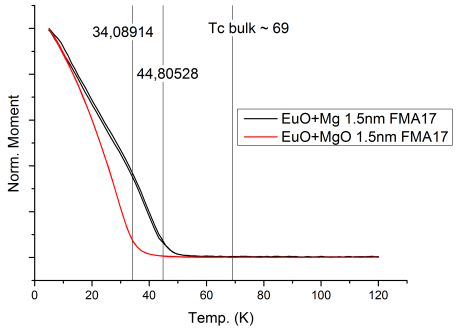

(d) $M(T)$ for FMA17 - 1.5nm

Figure 5.8: $M(T)$ for a selected set of samples

decreasing thickness of EuO layer, described in paragraph 2.3, is evident. But, as clear from the pictures, the Curie temperature of the EuO layers interfaced with Mg is always higher compared to the EuO layers interfaced with MgO. Samples interfaced with a polarizable media experience image charge screening, that modifies the parameters U and Δ involved in ferromagnetic exchange and therefore partially restore the magnetic ordering, leading to a higher T_C. Also, as the thickness decrease, the difference of the value of in the two different configurations becomes more evident, going from $\Delta T \approx 0$ K up to a value of $\Delta T \approx 10$ K for the 1.5 nm sample. The increasing difference in the value of T_C could be indeed the result of the interplay between the competing effects of reduced dimensionality and image charge screening. Fig. 5.9 shows graphically the increasing deviation in T_c behaviour as a function of the thickness for Eu/Mg and Eu/MgO. Scattered dots represent the experimental data, and the curves are a fitting of the data with an exponential function

of the type

$$T_C(t) = Ae^{-\frac{t}{\tau}} + T_0 \tag{5.15}$$

with adjustable parameters A, τ, T_0. A more detailed theoretical treatment and fitting can be found in Schiller et al. [30] and in Muller et al. [18] as described in chapter 2. The data show that a lowering of the magnetic ordering temperature in thin EuO films sets in for a thickness of around 50 Å for Eu films interfaced with MgO, but only for smaller thicknesses below ≈ 35 Å when interfaced with Mg metal.

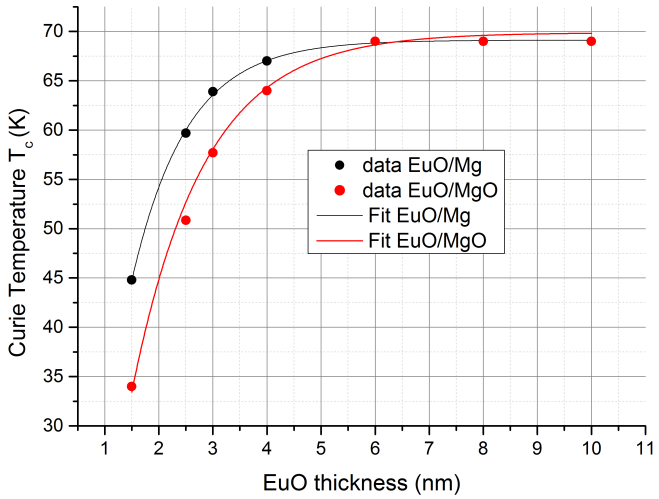

Figure 5.9: graphical representation of $T_C(t)$ dependence

5.2.2 Magnetization vs. Field - M(H)

After the observations on the $M(H)$ results of sample FMA08, for all the following samples we decided to acquire two $M(H)$ measaurements on the same sample piece, one at $T = 5$ K, below T_C where the ferromagnetic contribution of EuO is visible, and another one at $T = 80$ K (above T_C) where the signal due to the substrate should dominate. Fig. 5.11, 5.10, 5.12 show the results the $M(H)$ measurements for samples FMA15, FMA14 and FMA17 of 3nm, 2.5 nm and 1.5nm, respectively. All the samples clearly display the presence of a ferromagnetic behaviour at low temperature, for $T << T_C$. This means that a ferromagnetic EuO phase is present, and therefore the previously acquired measurements of the $M(T)$ behaviour are meaningful. All the signals recorded for $T > T_C$ show the expected diamagnetic behaviour, with a negative slope due to the negative overall magnetic susceptibility of the sample at high temperature. However, despite the order of magnitude is correct and the calculation in eq. 5.12 is just an approximation, none of the samples displays the theoretical saturation value $M_{sat,th} = 7\mu_B$. This might be explained by the

complex geometry, the competing magnetic signals and the oxided EuO edges.

We can clearly distinguish three different kind of behaviour, due to three possibile different situations that can affect the measurements.

In particular, we can group:

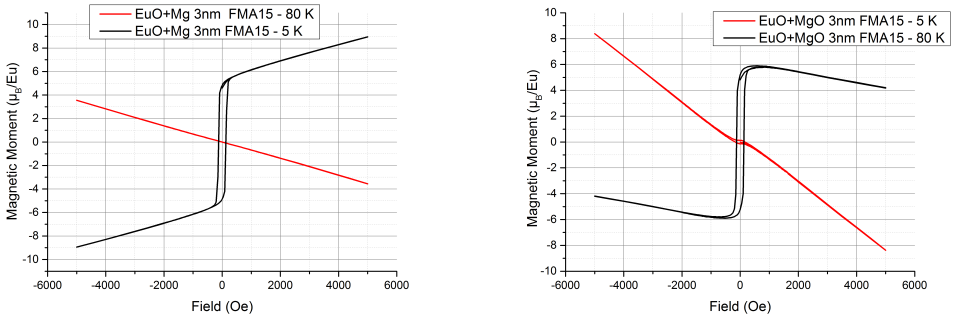

(a) $M(H)$ for EuO/Mg sample

(b) $M(H)$ for Eu/MgO sample

Figure 5.10: Results for $M(H)$ of sample FMA 15 (3 nm)

1) fig. 5.10(a) and fig. 5.11(a), with a saturation magnetization very close to the expected value $M_{sat,th} = 7\mu_B$, a superimposed paramagnetic value of Mg as expected and a correct linear dependency for $T > T_C$. Here, the small discrepancy between the theoretical and the experimental value of M_{sat} is probably due to a slightly wrong estimation of the sample volume, and of the cell volume due to the temperature-dependent value of a_{cell}. The oxidation of small parts of the sample edges might also play a role, reducing the effective volume of the sample contributing to the magnetic signal.

2) fig. 5.10(b) and fig. 5.12(b) shows both a saturation value slightly smaller than $M_{sat,th} = 7\mu_B$, and a superimposed linear and negative diamagnetic behaviour typical of the MgO layer and YSZ substrate. As before, the small difference between $M_{sat,th}$ and $M_{sat,exp}$ is probably due to a non perfect estimations of the value of the parameters in eq. 5.12.

3) fig. 5.11(b) and fig. 5.12(a) are similar, despite being the results of different sample configurations. Here the signals at $T > T_C$ are again negative, meaning that the overall behaviour is diamagnetic, but not linear. Moreover, the negative non-linear dependency is clearly visible also for the measurements at $T = 5$ K. We do not have yet a reliable explanation for such a behaviour, but it is highly probable that this is due to some contaminations and impurities already present in the substrate or deposited on the sample during the preparation, outside the chamber, of the sample pieces to be analyzed by the SQUID.

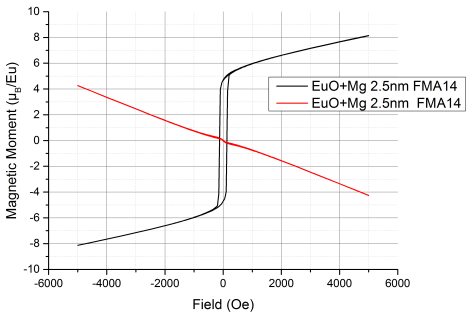

(a) $M(H)$ for EuO/Mg sample

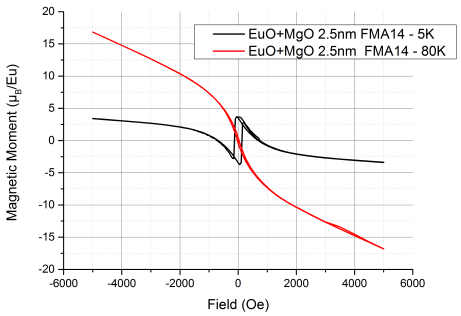

(b) $M(H)$ for Eu/MgO sample

Figure 5.11: Results for $M(H)$ of sample FMA 14 (2.5 nm)

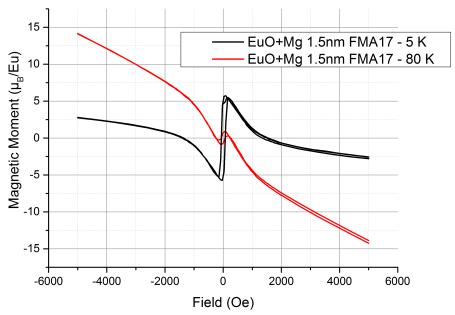

(a) $M(H)$ for EuO/Mg sample

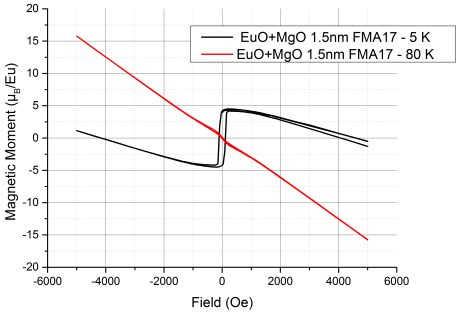

(b) $M(H)$ for Eu/MgO sample

Figure 5.12: Results for $M(H)$ of sample FMA 17 (1.5 nm)

6. Conclusions

This thesis ends with the magnetic measurements of the different samples, showing the interplay between reduced dimensionality and charge screening effects. These results were possible after the long and careful work done to optimize the recipe of the growth of EuO on YSZ, and the one for growing metal and metal oxides on the EuO surface. The problem of the overoxidation of EuO and its epitaxial growth turned out to be most challenging ones, but good results have been obtained on both sides. RHEED analysis was performed both in real-time and after the growth, to monitor the crystal quality and the thickness of the growing films.

The XPS analysis confirmed the desired stoichiometry both for pure EuO films and EuO/Mg/MgO films, with all the precaution described in chapter 4. A stable growth of both Mg and MgO has been achieved and a large amount of samples has been prepared.

XRR and HAXPES analysis were limited only to some particular samples. XRR was used to determine the sample thickness, that turned out to be in good agreement with the estimations based on RHEED oscillations, while HAXPES was used both to confirm the results of XPS and to test the possibility of future studies on EuO-based samples. Results were not completely satisfactory, because one of the two samples analyzed showed overoxidation after the shipment to the synchrotron facility in Japan. This aspect must be still investigated, different possibile capping layer (Au, Al) has been tested and are going to be tested in the future. In addition, an improved vacuum suitcase will be designed for the future experiments.

About the magnetic measurements, we obtained a good agreement between the literature [18] and our experimental data, as visible from the comparison between fig. 6.1(a) and fig. 6.1(b). The plots in fig 6.1 clearly show the differences between the values for T_C in samples interfaced with Mg metal and samples interfaced with MgO. These results suggest that the screening effect in proximity

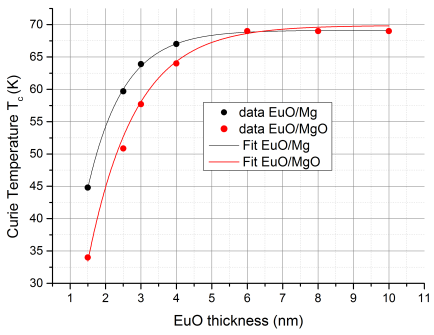

(a) $M(T)$ overview for Eu/MgO samples

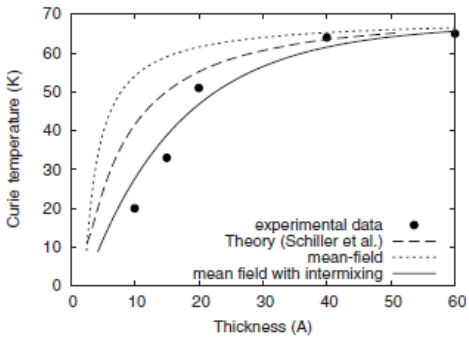

(b) $M(T)$ overview for Eu/MgO samples

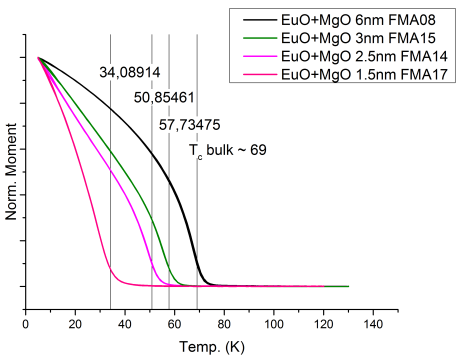

(c) $M(T)$ overview for Eu/MgO samples

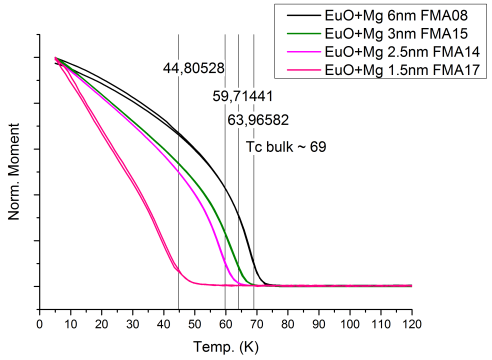

(d) $M(T)$ overview for Eu/Mg samples

Figure 6.1: Summary of the results of the M(T) dependence, for samples interfaced with MgO and Mg

to a polarizable material indeed has a considerable influence on the properties of a semiconducting layer. It seems to lower the energies for virtual charge excitations in the EuO layer which in turn causes an enhancement of the magnetic exchange interactions and thus an increase of T_C compared to an insulating material. The image charge screening effect is not strong enough to completely restore the bulk value of the Curie temperature in thin films, as clearly shown, but this is not the objective of the present research. Many different manipulations like dopings and oxygen vacancies were shown to be effective in enhancing the Curie temperature to value even higher than $T_C = 69$ K, even though they might have an effect on other properties of pure EuO like the metal-insulator transition (MIT) [13]. Instead, it is an important effect that must be studied and properly quantified when dealing with correlated systems interfaced with metals. In particular, the raising interest in building spin-FETs and correlated systems heterostructure would lead to situations where a full comprehension of this effect becomes crucial. The idea of image charge screening proposed by Duffy and Stoneham [36] and its application to correlated systems was able to explain very well the behaviour of T_C in EuO samples, giving useful indications for further studies. Our trials to get a clear ferromagnetic signal with the correct value of the saturation magnetization of $7\mu_B$ were not completely successful, and some open questions remains like the one related to the behaviour of samples FMA14 and FMA17 (fig.5.11(b) and fig. 5.12(a)). Further studies are needed to determine whether the root causes of the non-linear behaviour are just contaminations or interplay of different magnetic behaviours, as we suppose, and further tests are to be done to reach the desired magnetization value. Also, the edges of sensitive EuO samples might oxidize during the *ex-situ* experiments, and for the moment no definitive solutions to this problem have been found. In the end, the measurements of $M(H)$ shown in chapter 5 can be considered satisfactory, and a good basis for further research.

Bibliography

[1] B. T. Matthias, R. M. Bozorth, and J. H. Van Vleck. Ferromagnetic interaction in EuO. *Physical Review Letters*, 7(5):160–161, 1961.

[2] A Mauger and C Godart. The Magnetic, Optical, And Transport-Properties Of Representatives Of A Class Of Magnetic Semiconductors - The Europium Chalcogenides. *Physics Reports-Review Section Of Physics Letters*, 141(2-3):51–176, 1986.

[3] M. R. Oliver, J. O. Dimmock, and T. B. Reed. Temperature and Magnetic Field Dependence of the Conductivity of EuO. *IBM Journal of Research and Development*, 14(3):276–278, may 1970.

[4] A. Melville, T. Mairoser, A. Schmehl, T. Birol, T. Heeg, B. Hollaender, J. Schubert, C. J. Fennie, and D. G. Schlom. Effect of film thickness and biaxial strain on the curie temperature of EuO. *Applied Physics Letters*, 102(6):1–6, 2013.

[5] R. Sutarto, S. G. Altendorf, B. Coloru, M. Moretti Sala, T. Haupricht, C. F. Chang, Z. Hu, C. Schüßler-Langeheine, N. Hollmann, H. Kierspel, H. H. Hsieh, H. J. Lin, C. T. Chen, and L. H. Tjeng. Epitaxial and layer-by-layer growth of EuO thin films on yttria-stabilized cubic zirconia (001) using MBE distillation. *Physical Review B - Condensed Matter and Materials Physics*, 79(20):1–9, 2009.

[6] S. G. Altendorf, A. Efimenko, V. Oliana, H. Kierspel, A. D. Rata, and L. H. Tjeng. Oxygen off-stoichiometry and phase separation in EuO thin films. *Physical Review B*, 84(15):155442, oct 2011.

[7] Ronny Sutarto. *EuO and Gd - doped EuO thin films : epitaxial growth and properties*. PhD thesis, 2009.

[8] S. G. Altendorf, A. Reisner, C. F. Chang, N. Hollmann, A. D. Rata, and L. H. Tjeng. Growth and characterization of Sc-doped EuO thin films. *Applied Physics Letters*, 104(5):052403, feb 2014.

[9] A. Reisner, D. Kasinathan, S. Wirth, L. H. Tjeng, and S. G. Altendorf. Valence state of Sm in single-crystalline EuO thin films. *EPL (Europhysics Letters)*, 117(4):47001, feb 2017.

[10] T. Kasuya. Exchange Mechanisms in Europium Chalcogenides. *IBM Journal of Research and Development*, 14(3):214–223, may 1970.

[11] AA. VV. EuO: crystal structure, physical properties. In O. Madelung, U. Rossler, and M. Schulz, editors, *Non-Tetrahedrally Bonded Binary Compounds II*, pages 1–18. Springer-Verlag, Berlin/Heidelberg.

[12] Europium monoxide: [WebElements Periodic Table].

[13] M. Moretti Sala. *Magnetic and Transport Properties of EuO thin films*. PhD thesis, Politecnico di Milano, 2007.

[14] Wen-Yi Tong, Hang-Chen Ding, Yong-Chao Gao, Shi-Jing Gong, Xiangang Wan, and Chun-Gang Duan. Spin-dependent optical response of multiferroic EuO: First-principles DFT calculations. *Physical Review B*, 89(6):064404, feb 2014.

[15] T. Santos. Europium Oxide as a perfect electron spin filter. *PhD Thesis Massachusetts Institute of Technology, Department of Materials Science and Engineering*, 2007.

[16] G. Busch, P. Junod, and P. Wachter. Optical absorption of ferro- and antiferromagnetic europium chalcogenides. *Physics Letters*, 12(1):11–12, sep 1964.

[17] T. S. Santos, J. S. Moodera, K. V. Raman, E. Negusse, J. Holroyd, J. Dvorak, M. Liberati, Y. U. Idzerda, and E. Arenholz. Determining exchange splitting in a magnetic semiconductor by spin-filter tunneling. *Physical Review Letters*, 101(14):1–4, 2008.

[18] Martina Müller, Guo-Xing Miao, and Jagadeesh S. Moodera. Exchange splitting and bias-dependent transport in EuO spin filter tunnel barriers. *EPL (Europhysics Letters)*, 88(4):47006, nov 2009.

[19] C. Caspers, S. Flade, M. Gorgoi, A. Gloskovskii, W. Drube, C. M. Schneider, and M. Müller. Ultrathin magnetic oxide EuO films on Si(001) using SiOx passivation-Controlled by hard x-ray photoemission spectroscopy. *Journal of Applied Physics*, 113(17):17C505, may 2013.

[20] N.F. Mott. On the transition to the metallic conduction in semicondiuctors. *Canadian Journal of Physics*, 34(12A), 1956.

[21] David J. Griffiths. *Introduction to Quantum Mechanics, 2nd ed.* Prentice Hall, 2005.

[22] John Hubbard. Electron Correlations in Narrow Energy Bands. *Proceedings of the Royal Society of London Series*, 276:238–257, 1963.

[23] R. Hesper, L. H. Tjeng, and G. A. Sawatzky. Strongly reduced band gap in a correlated insulator in close proximity to a metal. *Europhys. Lett*, 40:177–182, 1997.

[24] V Ramachandran and R M Feenstra. Scanning tunneling spectroscopy of Mott-Hubbard states on the 6H-SiC(0001) surface. *Physical Review Letters*, 82(5):1000–1003, 1999.

[25] E Koch. *Strongly Correlated Electrons: Exchange Mechanisms*, volume 7. 2012.

[26] J. B. Goodenough. Theory of the role of covalence in the perovskite-type manganites [La,M(II)]MnO. *Physical Review*, 100(2):564–573, 1955.

[27] J. B. Goodenough. Goodenough-Kanamori Rules, 2008.

[28] J. M. D. Coey. *Magnetism and magnetic materials*. Cambridge University Press, 2009.

[29] Dalía S. Bertoldi, Eduardo M. Bringa, and E. N. Miranda. Analytical solution of the mean field Ising model for finite systems. *Journal of Physics: Condensed Matter*, 24(22):226004, jun 2012.

[30] R. Schiller and W. Nolting. Thickness dependent Curie temperatures of ferromagnetic Heisenberg films. *Solid State Communications*, 110(2):121–125, 1999.

[31] R. Schiller and W. Nolting. Prediction of a surface state and a related surface insulator-metal transition for the (100) surface of stochiometric EuO. *Physical Review Letters*, 86(17):3847–3850, 2001.

[32] Ezana Negusse, J. Holroyd, M. Liberati, J. Dvorak, Y. U. Idzerda, T. S. Santos, J. S. Moodera, and E. Arenholz. Effect of electrode and EuO thickness on EuO-electrode interface in tunneling spin filter. *Journal of Applied Physics*, 99(8):08E507, apr 2006.

[33] S. Altieri, L. H. Tjeng, and G. A. Sawatzky. Ultrathin oxide films on metals: New physics and new chemistry? *Thin Solid Films*, 400(1-2):9–15, 2001.

[34] S Altieri, L H Tjeng, F C Voogt, T Hibma, O Rogojanu, and G A Sawatzky. Charge fluctuations and image potential at oxide-metal interfaces. *Phys. Rev. B*, 66(15):155432, 2002.

[35] S. Altieri, M. Finazzi, H. H. Hsieh, M. W. Haverkort, H. J. Lin, C. T. Chen, S. Frabboni, G. C. Gazzadi, A. Rota, S. Valeri, and L. H. Tjeng. Image charge screening: A new approach to enhance magnetic ordering temperatures in ultrathin correlated oxide films. *Physical Review B - Condensed Matter and Materials Physics*, 79(17):1–6, 2009.

[36] D. M. Duffy and A. M. Stoneham. Conductivity and 'negative U' for ionic grain boundaries. *Journal of Physics C: Solid State Physics*, 16(21):4087–4092, jul 1983.

[37] Salvatore Altieri. Electronic structure of oxide thin films on metals., 1999.

[38] W. Patrick McCray. MBE deserves a place in the history books. *Nature Nanotechnology*, 2(5):259–261, 2007.

[39] Marian A. Herman and Helmut Sitter. *Molecular Beam Epitaxy : Fundamentals and Current Status*. Springer Berlin Heidelberg, 1996.

[40] Hans Lüth. *Surfaces and Interfaces of Solid Materials*. Springer-Verlag Berlin Heidelberg, 1995.

[41] Wikipedia. Stranski-Krastanov growth, 2017.

[42] John E. Ayers, Tedi Kujofsa, Paul Rango, and Johanna E. Raphael. *Heteroepitaxy of semiconductors : theory, growth, and characterization*.

[43] P. G. Steeneken. *New light on EuO thin films: preparation, transport, magnetism and spectroscopy of a ferromagnetic semiconductor*. 2012.

[44] Neil. W. Ashcroft and David N. Mermin. *Solid State Physics*. Saunders, 1976.

[45] Lamberto Duò and Alberto Brambilla. Introduzione alle Spettroscopie Elettroniche. page 58, 2013.

[46] M. P. Seah and W. A. Dench. Quantitative electron spectroscopy of surfaces: A standard data base for electron inelastic mean free paths in solids. *Surface and Interface Analysis*, 1(1):2–11, 1979.

[47] J. N. Beukers, J. E. Kleibeuker, G. Koster, D. H. Blank, G. Rijnders, H. Hilgenkamp, and A. Brinkman. Epitaxial EuO thin films by pulsed laser deposition monitored by in situ x-ray photoelectron spectroscopy. *Thin Solid Films*, 518(18):5173–5176, 2010.

[48] W. H. Hocking and J. A. D. Matthew. Electron spectroscopy of europium. *Journal of Physics: Condensed Matter*, 2(15):3643, 1990.

[49] Johnathon Holroyd, Y. U. Idzerda, and Shane Stadler. Properties of thin film europium oxide by x-ray magnetic circular dichroism. *Journal of Applied Physics*, 95(11), 2004.

[50] Raghava P. Panguluri, T. S. Santos, E. Negusse, J. Dvorak, Y. Idzerda, J. S. Moodera, and B. Nadgorny. Half-metallicity in europium oxide conductively matched with silicon. *Physical Review B*, 78(12):125307, sep 2008.

[51] A. G. Swartz, J. Ciraldo, J. J. I. Wong, Yan Li, Wei Han, Tao Lin, S. Mack, J. Shi, D. D. Awschalom, and R. K. Kawakami. Epitaxial EuO Thin Films on GaAs. *Applied Physics Letters*, 97(11), 2010.

[52] John David Jackson. *Classical Electrodynamics, 3rd Edition*. John Wiley and Sons, 1998.

[53] Mario Birkholz, Paul F. Fewster, and Christoph. Genzel. *Thin film analysis by X-ray scattering*. Wiley-VCH, 2006.

[54] Miho Yasaka. X-ray thin-film measurement techniques. *The Rigaku Journal*, 26(2):1–9, 2010.

[55] Leon N. Cooper. Bound Electron Pairs in a Degenerate Fermi Gas. *Physical Review*, 104(4):1189–1190, nov 1956.

[56] Charles Kittel. *Introduction to solid state physics*, volume Third. John Wiley & Sons, Inc, 7 edition, 1953.

[57] J. Q. You and Franco Nori. Atomic physics and quantum optics using superconducting circuits. *Nature*, 474(7353):589–597, jun 2011.

[58] San Jose State University: http://www.sjsu.edu/people/raymond.kwok/courses/physics/phys120s-lab/squid/.

[59] B. Coloru. *Epitaxial and layer-by-layer growth of pure and doped EuO thin films on YSZ (001)*. PhD thesis, Politecnico di Milano, 2008.

[60] Robert C. Weast and Lide David R. Handbook of chemistry and physics, 1978.